

# POLITECNICO DI TORINO

## MASTER's Degree in BIOMEDICAL ENGINEERING



## Politecnico di Torino

MASTER's Degree Thesis

# Impedance Plethysmography: a novel technique for Pulse Wave Detection

Supervisors

Prof. DANILO DEMARCHI

Ph.D. IRENE BURAIOLI

Ph.D. ALESSANDRO SANGINARIO

Ph.D. St. MARCO POGLIANO

Candidate

**CAROLINA SERA**

MARZO 2025



# Summary

Cardiovascular diseases (CVDs) remain the leading cause of death globally, accounting for approximately 30% of annual fatalities. Addressing this persistent public health challenge requires the development of effective strategies for prevention, early diagnosis, and management.

A critical marker of cardiovascular health is arterial stiffness, typically assessed through Pulse Wave Velocity (PWV). Current PWV measurement methods involve acquiring Pulse Wave (PW) signals from two anatomical sites, commonly the carotid and femoral arteries, using tonometers and measuring the pulse arrival time to compute the velocity. While these devices are widely used in clinical practice, they are hindered by several inherent limitations, including an inability to support continuous monitoring and a reliance on operator skill to maintain proper sensor placement over the artery during measurement.

Impedance Plethysmography (IPG) shows great potential as an alternative technology for developing wearable devices that enable continuous, non-invasive monitoring of arterial stiffness. The aim of this thesis is to demonstrate the feasibility of creating a novel IPG-based device for measuring PWV. By injecting a fixed alternating current into a tissue region crossed by an artery and measuring the resulting voltage drop, it is possible to infer the variation in the electrical impedance of the vessel, related to changes in blood flow.

The core of the impedance measurement system is the Howland Current Pump (HCP), which is known for providing a stable output alternating current when a voltage signal is applied at the input. Signal acquisition was carried out using the NiDAQ USB-6259 acquisition board, which provides a high sampling rate essential for accurately demodulating the signal. Prior to in-vivo validation, the hardware's performance was tested to ensure a stable and safe output current. A MATLAB<sup>®</sup> App Designer-based Graphical User Interface (GUI) was developed for real-time raw signal processing and impedance visualization, improving electrode placement efficiency. It allows the user to adjust both the sampling frequency and the characteristics of the HCP input waveform. The GUI also includes a toolbox for saving data. The integration of each component into the system was carried

out with the objective of reducing noise in the acquired signal. To this end, shorter cables were utilized for the connection of the HCP hardware to the electrodes, thereby minimizing the distance to the skin. Furthermore, a voltage follower was placed between the electrodes and the analog input of the acquisition board, to prevent signal dispersion along the cables.

The in-vivo validation test was performed by acquiring the subject's ECG signal in order to confirm the relation between the pulse wave and heart contraction activity. While the system supports signal acquisition from two arterial sites for the calculation of pulse wave velocity, the test focused solely on the carotid artery due to the difficulty in accessing the femoral artery.

The results demonstrate the effectiveness of applying the IPG principle to Pulse Wave detection, offering a non-invasive, real-time method for monitoring cardiovascular health. Despite these promising outcomes, electrode placement and subject variability remain challenges for future development, serving as a starting point for adopting a multi-electrode approach that will reduce the need for precise placement and mitigate the effects of variability.

# Acknowledgements

*A mio padre*



# Table of Contents

<b>List of Tables</b>	VIII
<b>List of Figures</b>	IX
<b>Acronyms</b>	XIII
<b>1 Introduction</b>	1
<b>2 Background</b>	5
2.1 The cardiovascular system . . . . .	5
2.1.1 Heart . . . . .	7
2.1.2 Blood vessels . . . . .	15
2.1.3 Blood . . . . .	20
2.2 Cardiovascular diseases . . . . .	23
2.2.1 Hypertension and Arterial stiffnes . . . . .	24
2.3 Pulse Wave Velocity . . . . .	26
2.3.1 Pulse Wave . . . . .	26
2.3.2 PWV estimation . . . . .	27
2.3.3 Clinical devices for PWV estimation . . . . .	29
2.4 Impedance Plethysmography . . . . .	34
2.4.1 IPG application to PWV estimation: a state of the art . . .	37
<b>3 Materials</b>	38
3.1 Impedance measurement system . . . . .	38
3.1.1 Howland Current Pump (HCP) . . . . .	40
3.1.2 NiDAQ USB-6259 . . . . .	43
3.2 E4990A Impedance Analyzer . . . . .	44
3.3 Biosignalplux ECG . . . . .	45
<b>4 Hardware Design</b>	47
4.1 Estimation of Load Impedance . . . . .	47

4.1.1	Methods and Results . . . . .	47
4.2	Howland current pump (HCP) design . . . . .	50
4.3	Printed circuit board (PCB) design . . . . .	52
4.4	HCP validation test . . . . .	53
4.4.1	Results of HCP validation test . . . . .	54
4.5	Hardware assembly . . . . .	56
<b>5</b>	<b>System implementation</b>	<b>57</b>
5.1	Impedance processing . . . . .	57
5.1.1	Real time signal processing . . . . .	59
<b>6</b>	<b>In Vivo Experimental Validation</b>	<b>61</b>
6.1	Preliminary Analysis . . . . .	61
6.2	Algorithms . . . . .	62
6.2.1	Intersecting Tangent Point Algorithm . . . . .	62
6.2.2	Pan-Tompkins Algorithm . . . . .	64
6.3	Experimental protocol . . . . .	66
6.4	Data processing . . . . .	67
6.5	Results and statistical analysis . . . . .	68
<b>7</b>	<b>Conclusion</b>	<b>71</b>
<b>A</b>	<b>Schematic</b>	<b>72</b>
	<b>Bibliography</b>	<b>75</b>

# List of Tables

4.1	Table of resistor and capacitor values of the circuit in Figure 4.3. . .	51
-----	--	----

# List of Figures

1.1	Types of heart disease and risk factors [2]. . . . .	1
1.2	Graphical representation of carotid-femoral pulse wave velocity (cf-PWV). The PTT is calculated as the time delay between the proximal pressure waveform and the distal pressure waveform [6]. . . . .	3
2.1	The path of blood flow through the cardiovascular system [11]. . . .	6
2.2	Blood flow patterns in the cardiovascular system [12]. . . . .	7
2.3	A cutaway view of the heart, exhibiting the atria, ventricles, atrioventricular valves, and their interconnection with the principal blood vessels [11]. . . . .	8
2.4	Right and left ventricle muscle thickness [11]. . . . .	8
2.5	Heart conduction system [11]. . . . .	10
2.6	The spread of the action potentials through the heart [11]. . . . .	11
2.7	Einthoven's triangle and Goldberger's leads [13]. . . . .	12
2.8	Anatomical placement of precordial leads [13]. . . . .	13
2.9	Electrocardiogram recording [14]. . . . .	13
2.10	Illustration of cardiac cycle, the given values are referred to the left heart. It is possible to observe the relationship between changes in pressure gradient across the valves and the state of the valves themselves (open or closed), as well as the changes in the volume of the ventricles. Heart sounds are linked to the valves closing, while ECG waves are connected to the heart's mechanical actions [11]. . .	16
2.11	Blood vessels type [11]. . . . .	17
2.12	The role of arteries as a pressure reservoir [11]. . . . .	18
2.13	Following centrifugation, a blood sample is obtained for composition analysis [11]. . . . .	20
2.14	Hemoglobin [15]. . . . .	21
2.15	Number of CVD Deaths from 1990-2019 by Sex [3]. . . . .	23
2.16	Lesion types of atherosclerosis [16]. . . . .	25
2.17	Carotid pulse waveform. . . . .	27
2.18	Carotid-femoral Pulse Transit Time estimation. . . . .	28

2.19	PWV measurements based on imaging technique. A) MRI at the aortic arch [22] ; B) US at femoral artery synchronized with ECG [23].	30
2.20	Illustration of the SphygmoCor device [24].	31
2.21	Illustration of the PulsePen device [25].	31
2.22	Illustration of the Complior Analyse device [26].	32
2.23	Illustration of the Arteriograph device [27].	33
2.24	ATHOS system overview and details of the probe [29].	33
2.25	Impedance model of the blood and its surrounding tissue.	35
2.26	Electrodes placement for IPG acquisition. Outer (excitation) electrodes inject current and inner (sensing) electrodes measure the voltage. (a) Parallel and (b) Transversal configuration.	36
2.27	IPG waveform [34].	36
3.1	Impedance measurement system. The yellow box represents the Howland current pump, which acts as a voltage-controlled current source, injecting a constant alternating current into the tissues. The NiDAQ USB-6259 then acquires the voltage signal between the inner electrodes, which is generated by the current flow through the tissue and its impedance. The voltage followers, depicted in the green box, are placed between the electrodes and the ADC to ensure signal integrity by preventing loading effects and minimizing distortion.	39
3.2	Standard pre-gelled and self-adhesive disposable electrodes and ECG cables.	40
3.3	Basic Howland Current Pump.	40
3.4	Improved Howland current pump.	42
3.5	NiDAQ USB-6259	43
3.6	E4990A Impedance Analyzer Keysight Technologies [39].	44
3.7	8-Channel <i>biosignalsplux</i> kit	45
3.8	(a) Standard biosignalsplux ECG sensor with short electrode cables (4cm + 6cm + 4cm) and (b) example sensor placement using an ECG triod (equivalent to a standard medical-grade V6 lead) [41].	46
4.1	Frequency-dependent impedance trend for two different testing distances (5 cm, 12 cm), the dashed line indicates the frequency of the applied current signal.	49
4.2	High and low frequency current distributions in cell suspensions [43].	49
4.3	Configuration of the developed Improved Howland Current Pump which includes the feedback capacitor.	51
4.4	PCB layout showing an overview of (a) the top layer and (b) the bottom layer. The main components are highlighted in red.	52

4.5	Theoretical vs. real behavior of the HCP using the LT1498, with an input voltage of 5 V amplitude at a frequency of 50 kHz. . . . .	54
4.6	Theoretical vs. real behavior of the HCP using the LT1498, with an input voltage of 5 V amplitude at a frequency of 20 kHz. . . . .	55
4.7	Theoretical vs. real behavior of the HCP using the OPA2892, with an input voltage of 5 V amplitude at a frequency of 20 kHz. . . . .	55
5.1	Main window of the implemented GUI, displaying the saving toolbox, pulse wave graphs, and acquisition controls. The <i>Trigger</i> and <i>Invert</i> switches are highlighted in red. . . . .	58
5.2	The image illustrates how the GUI reads the incoming data buffer, processes it in real-time, and displays the impedance variation signal. . . . .	59
6.1	Minimums identification in the window $\pm\frac{T}{3}$ , centered in the <i>event starter</i> [28]. . . . .	62
6.2	ITP definition as the projection on the signal of the intersection point between the tangent at the maximum of the first derivate and the horizontal line passing through the minimum [28]. . . . .	63
6.3	Intermediate results of Pan-Tompkins Algorithm pre-processing stage. . . . .	65
6.4	Final results of QRS detection using an adaptive threshold, green line in the graphs. . . . .	65
6.5	In vivo test: recording setup. The main components of the setup are highlighted in red. . . . .	66
6.6	IPG electrodes placement: the excitation electrodes are the outer coloured of white, while the sensing electrodes are the inner red and black. . . . .	67
6.7	The recorded ECG and IPG signals are shown, along with the key parameters that were extracted. . . . .	69
6.8	Boxplots of Pulse Arrival Time (PAT) measurements for each subject. . . . .	69
6.9	Boxplots RR-PP. . . . .	70



# Acronyms

**CVS**

Cardiovascular System

**AV**

AtrioVentricular

**SA**

SinoAtrial

**LV**

Left Ventricle

**LDL**

Low Density Lipoprotein

**LAS**

Large Arterial Stiffness

**US**

UltraSound

**MRI**

Magnetic Resonance Imaging

**HF**

Heart Failure

**ECG**

Eletrocardiogram

**PWV**

Pulse Wave Velocity

**PW**

Pulse Wave

**PTT**

Pulse Transit Time

**CVDs**

Cardiovascular Diseases

**AO**

Analog Output

**AI**

Analog Input

**IPG**

Impedance Plethysmography

**AC**

Alternating Current

**WHO**

World Health Organization

**PCB**

Printed Circuit Board

**GUI**

Graphical User Interface

**CMRR**

Common-mode Rejection Ratio

**GBWP**

Gain Bandwidth Product

**HCP**

Howland Current Pump

**ECF**

Extracellular Fluid

**ICF**

Intracellular Fluid

**IED**

Inter-Electrode Distance

**ADC**

Analog to Digital Converter

# Chapter 1

## Introduction

Cardiovascular diseases (CVDs) are a class of diseases of the heart and blood vessels (Figure 1.1) that are the leading cause of death on a global scale. According to the World Health Organization (WHO), cardiovascular diseases account for 30% of total annual deaths [1].

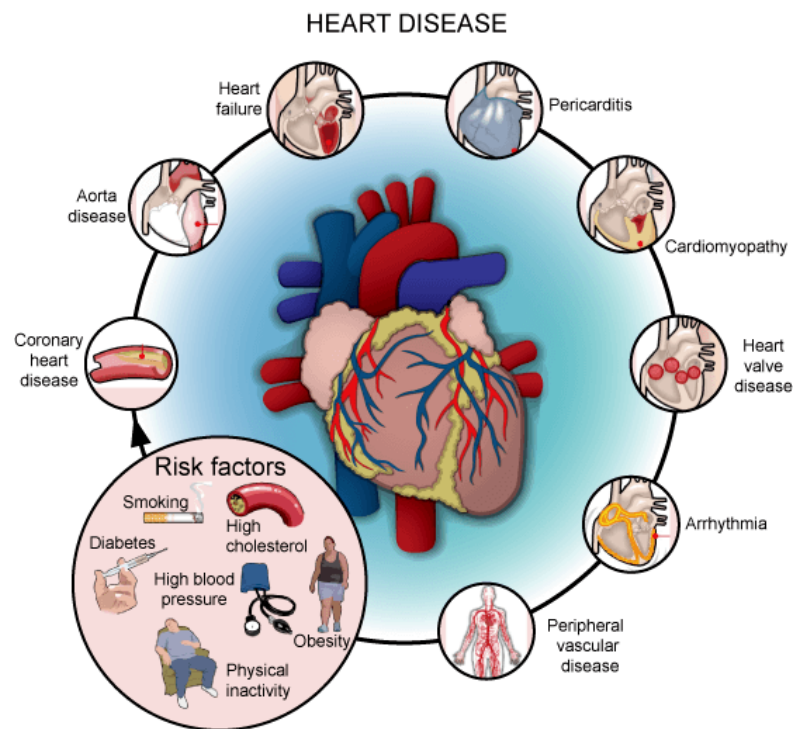


**Figure 1.1:** Types of heart disease and risk factors [2].

The prevalence has continued to rise over the years, highlighting a growing

and persistent challenge to global public health. For that reason, it is critical to employ feasible and cost-effective strategies aimed at preventing, diagnosing early, and managing the risk factors. Most cardiovascular diseases can be prevented by addressing behavioral predisposing factors such as tobacco use, unhealthy diet and obesity, physical inactivity and harmful use of alcohol using population-wide strategies. Although major advances have been made in the treatment of end-stage CVDs, research on ways to prevent the onset and progression of disease requires additional investments [3].

A strictly correlated parameter with the state of the cardiovascular system is the arterial stiffness which refers to the reduced ability of the arteries to expand and contract as blood flows through them. This process is influenced by a range of factors, including aging, genetic predisposition, and hypertension. The condition is also closely associated with atherosclerosis, where plaque buildup further contributes to reduced arterial flexibility elevating the risk of heart attack or stroke [4].

One way to assess the elastic property of the arterial tree is the Pulse Wave Velocity (PWV), that corresponds to the velocity at which blood pulse propagates through the cardiovascular system. In younger, healthier arteries that are more elastic, the pulse wave moves more slowly. However, when the arteries become stiffer, the pulse wave travels faster, which leads to a higher PWV. The evident relevance of this biomarker in the early prevention of cardiovascular risk leads to the development of many technologies for non-invasive measurement. Threaded catheterization during angiography is the most accurate method for measuring aortic PWV, but its invasive nature limits its use to specific cardiac or vascular diagnostic procedures [5].

PWV is calculated by dividing the distance between two arterial sensors by the time required for the wave to travel this distance (see Figure 1.2), referred to as Pulse Transit Time (PTT). The current clinical devices for the PWV measurement feature of tonometric sensors, this approach needs holding or mechanical fixation of a probe above the artery during measurement, where operating skills affect the evaluation and a trained operator is needed. Moreover, these devices are not wearable and do not permit continuous monitoring of PWV [5].

Other technologies have been investigated to overcome the limitations of existing devices, among which impedance plethysmography (IPG) is the focus of research. Impedance plethysmography (IPG) is a non-invasive technique that assesses changes in the electrical impedance of an artery, which are influenced by variations in blood flow. It works by applying a fixed alternating current (AC) through the tissues surrounding the vessel being investigated, and then measuring the resulting voltage drop to capture the pulse waveform [7].

The potential of impedance plethysmography in evaluating vascular health has

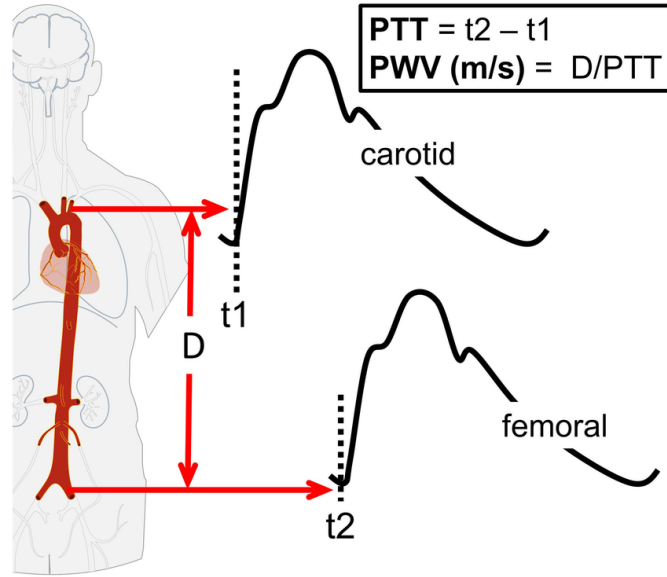


**Figure 1.2:** Graphical representation of carotid-femoral pulse wave velocity (cfPWV). The PTT is calculated as the time delay between the proximal pressure waveform and the distal pressure waveform [6].

prompted several feasibility studies focused on assessing the technique’s accuracy and practicality in clinical applications [8, 9, 10]. The aim of this project is to demonstrate the feasibility of applying the new methodology to the estimation of PWV.

A novel device was developed, beginning with the design of the current injection system. For this purpose, a waveform generator and a Howland current pump were used, with the resistance values appropriately chosen to ensure the desired output current while complying with electrical safety regulations. A thorough investigation of the Howland current pump operational amplifier was conducted to identify the one with the most suitable gain-bandwidth product (GBWP) relative to the frequency of the AC output current. The designed circuit was implemented on a printed circuit board (PCB) to miniaturize the hardware, allowing it to be conveniently placed near the collection site. The PCB is equipped with connectors for easy attachment of electrodes via cables, ensuring a compact and efficient setup for signal acquisition.

The signal acquisition was performed using a National Instruments data acquisition board (NI DAQ USB-6259), which ensures a high sampling rate, crucial for appropriately demodulating the signal. The analog output of the acquisition board acts as the input to the waveform generator, which controls the output current of the Howland current pump.

Using the MATLAB App Designer, a Graphical User Interface (GUI) was developed to process the raw signal in real time, allowing the final impedance signal to be visualized, thus facilitating and reducing the time required for electrode placement. Additional functionalities are included in the GUI, allowing the user to adjust the sampling frequency of signal acquisition or modify the characteristics of the output waveform. A data saving toolbox is also provided.

Although the implemented system allows simultaneous acquisition from two arterial sites, validation tests were performed only on the carotid site due to its enhanced accessibility. Finally, the correlation between the IPG signal and ECG signal is proved through statistical analysis of the results, demonstrating the feasibility of this methodology for PW detection.

The development of the novel device in this project represents a significant step toward overcoming the limitations of existing PWV measurement techniques. The successful implementation of this system paves the way for future design of wearable device, with the potential to enhance early detection and management of cardiovascular diseases. Further validation and improvement will be essential for broader clinical adoption and application.

# Chapter 2

## Background

This section provides a detailed overview of cardiovascular physiology and outlines the most prevalent cardiovascular diseases. It highlights the importance of pulse wave velocity (PWV) as an important biomarker of cardiovascular health and reviews the devices currently available to measure PWV. After discussing the limitations of clinical methods used to assess PWV, a novel technique is presented and described.

### 2.1 The cardiovascular system

The integrated actions of the organ system enable cells to survive in a stable internal environment. The cardiovascular system (CVS) plays a pivotal role in maintaining homeostasis despite external changes. The CVS is responsible for the transportation of nutrients and oxygen to cells, as well as the delivery of waste products and carbon dioxide to organ systems for elimination from the body. The interstitial fluid facilitates the exchange of materials between the extracellular space and the cell through the process of diffusion [11].

The cardiovascular system is also fundamental to thermoregulation and the distribution of hormones throughout the body, thereby facilitating effective communication and control of various physiological functions [11]. The cardiovascular system is constituted by the heart, which pumps blood through the vessels, including arteries, capillaries, and veins. The heart and vessels function in an integrated manner to ensure adequate blood flow to all body parts.

The vessel system is subdivided into two discrete circulatory pathways: the pulmonary circulation, which includes all blood vessels within the lungs as well as those connecting the lungs with the heart, and the systemic circulation, which comprises the rest of the blood vessels in the body (see Figure 2.1).

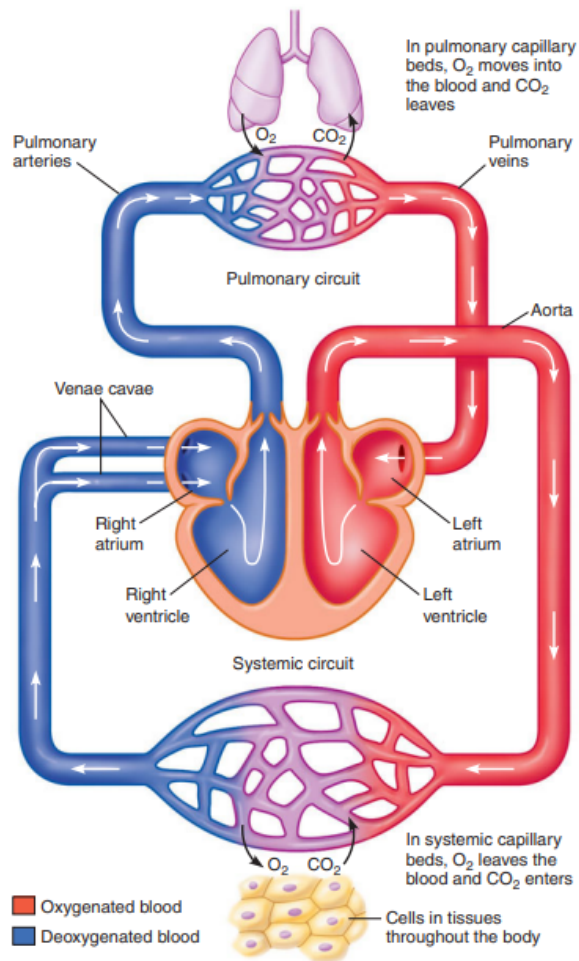


**Figure 2.1:** The path of blood flow through the cardiovascular system [11].

The Figure 2.2 illustrates why blood flow in the systemic circuit is referred to as parallel flow. In this system, blood does not flow directly from one organ to the next. Instead, it is distributed through a network of vessels that supply blood to multiple organs simultaneously. This parallel arrangement allows each organ to receive blood based on its individual needs, without influencing the blood flow to other organs. As a result, this system provides a highly efficient way to meet the varying demands of different tissues throughout the body [12].

The right side of the heart collects deoxygenated blood, which is then supplied to the pulmonary circuit. In the capillary beds of the lungs, oxygen flows into the blood from air, while carbon dioxide leaves the blood. When it returns to the left side of the heart, the blood is relatively rich in oxygen and is pumped in the systemic circulation. In the systemic capillaries, oxygen leaves the blood and moves

to cells, while carbon dioxide enters the vessel [11].

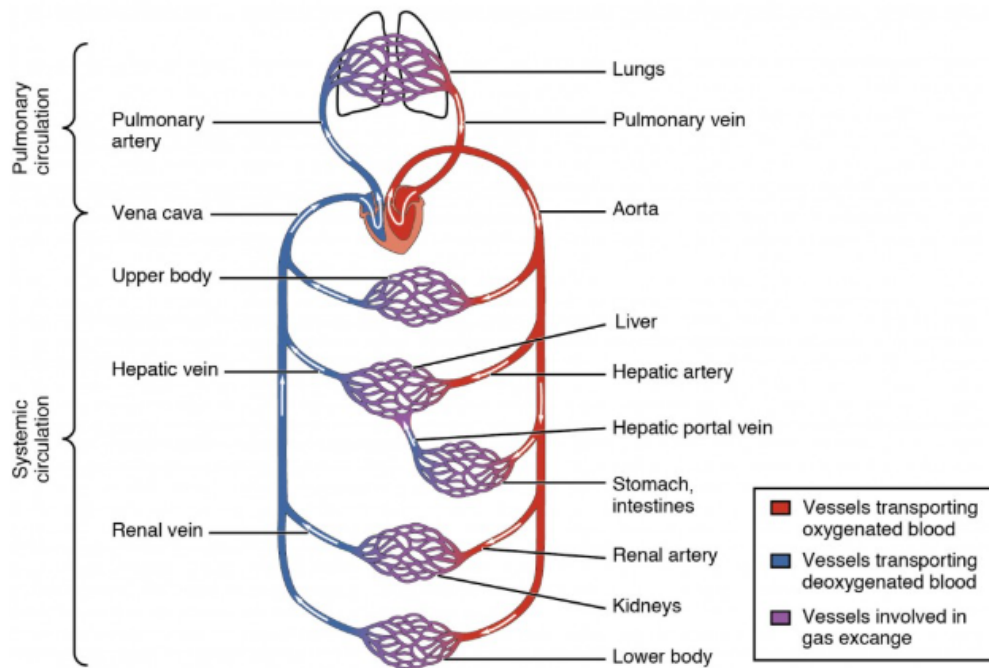


**Figure 2.2:** Blood flow patterns in the cardiovascular system [12].

### 2.1.1 Heart

The heart is the muscular pump that generates the force necessary to propel blood through the vasculature. The heart is situated within the thoracic cavity, in a medial position between the lungs, within the space designated as the mediastinum. The heart is approximately the size of a fist and is encased in a membrane called the pericardium, which contains a fluid that reduces the friction experienced as the heart contracts and relaxes.

The heart contains four distinct chambers (see Figure 2.3): two upper chambers, the atria, which collect the blood that moves to the heart, and two lower chambers, the ventricles, which receive the blood from the atria and push it away from the heart through the blood vessels. The left ventricle is the thickest chamber as shown in Figure 2.4 because it pumps blood throughout the body at high pressure, whereas the right ventricle only needs to pump the blood to the lungs, which are in close proximity. The septum of the heart is a wall of tissue that separates the left and right sides of the heart, preventing the mixing of blood in the left heart with that in the right heart.

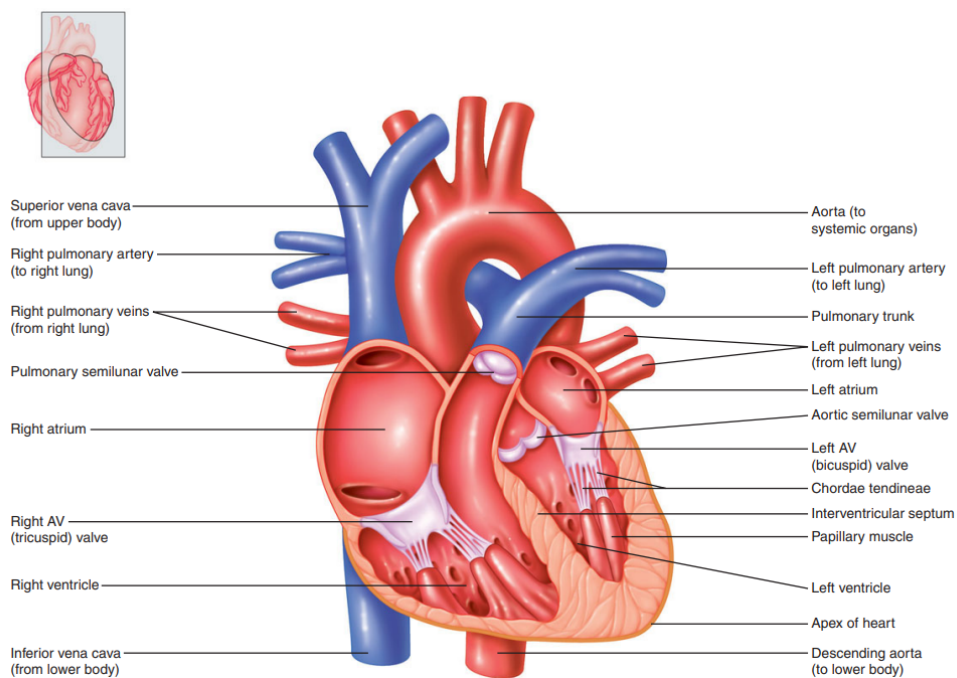


**Figure 2.3:** A cutaway view of the heart, exhibiting the atria, ventricles, atrioventricular valves, and their interconnection with the principal blood vessels [11]

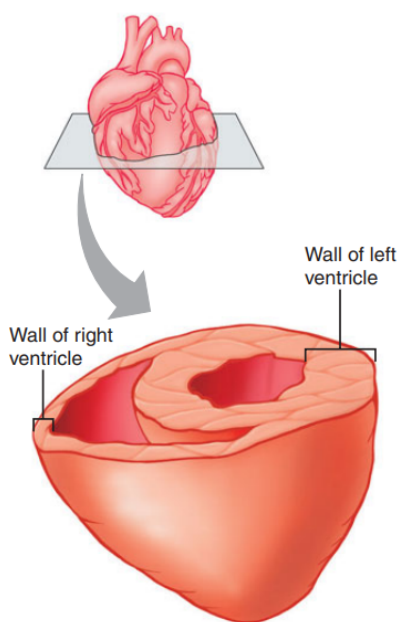


**Figure 2.4:** Right and left ventricle muscle thickness [11].

The heart wall is comprised of three distinct layers. The cardiac muscle forms a thick middle layer between the outer layer of connective tissue, designated as the epicardium, and an inner layer of epithelial cells, known as the endothelium.

The rhythmic contraction and relaxation of the myocardium enables the heart to perform its pump function. The contraction results in the wall moving inwards and the compression of the blood, which increases the pressure within the chamber and forces the blood out.

Four valves within the heart anatomy ensure unidirectional blood flow. These valves are located within the heart itself and between the heart and the blood vessels connected directly to it. The atrioventricular (AV) valves separate the atrium and ventricle on each side. The left AV valve is composed of two flaps of connective tissue, which is why it is referred to as the bicuspid valve or mitral valve. In contrast, the right AV valve has three cusps, which is why it is known as the tricuspid valve. AV valves exhibit a passive opening or closing response to cyclic fluctuations in pressure that occur with each heartbeat. During the contraction of the ventricles, the elevated pressure can result in the prolapse of the valves. To prevent this potentially dangerous phenomenon, the cusps are held in place by chordae tendinae, which are strands of connective tissue that extend from the edges of the cusps to the papillary muscles. The contractile force generated by the papillary muscles on the cusps through the chordae tendinae can serve to balance the pressure exerted by the blood on the valve in the opposite direction [11]. The remaining two valves are situated between the ventricles and the arteries. In the left heart, the aortic valve separates the left ventricle from the aorta, while in the right heart, the pulmonary valve is located between the right ventricle and the pulmonary artery.

The heart requires high level of oxygen that is supplied by the blood via the coronary arteries because the blood within the heart chambers can't provide significant quantities of nourishment.

### **Electrical heart activity**

The contractions of the cardiac muscle are triggered by signals that originate from a small percentage of muscle cells, which are known as autorhythmic cells. These cells can be divided into two categories: pacemaker cells, which spontaneously generate the electrical impulses that establish the heart rhythm, and conduction fibers, which propagate the signals through the heart.

Pacemaker cells are concentrated in two regions of the myocardium: the sinoatrial node (SA node), which is located in the wall of the right atrium, and the atrioventricular node (AV node), which is situated near the tricuspid valve in the interatrial septum as shown in Figure 2.5.

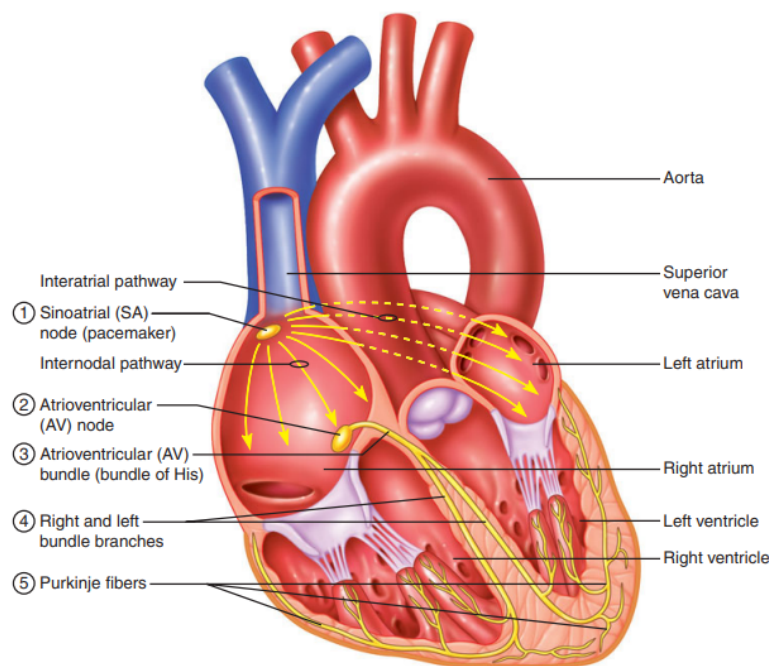


**Figure 2.5:** Heart conduction system [11].

The heart rate is established by the SA node due to its faster spontaneous depolarisation rate and the fact that it is connected to the AV node via conduction fibers. An action potential (see Figure 2.6) that originates in the SA node progresses to the AV node and subsequently disseminates throughout the majority of the atrial muscle. The propagation of the impulse is delayed by the cells of the AV node, thereby ensuring that the atrial contraction is complete before the onset of ventricular contraction. Subsequently, the electrical signal is conducted from the AV node to the ventricular myocardium via the bundle of His, which then splits into the left and right bundle branches after a short distance. The impulse then travels from the apex towards the valves via the Purkinje fibres, thereby initiating the ventricular contraction [11].

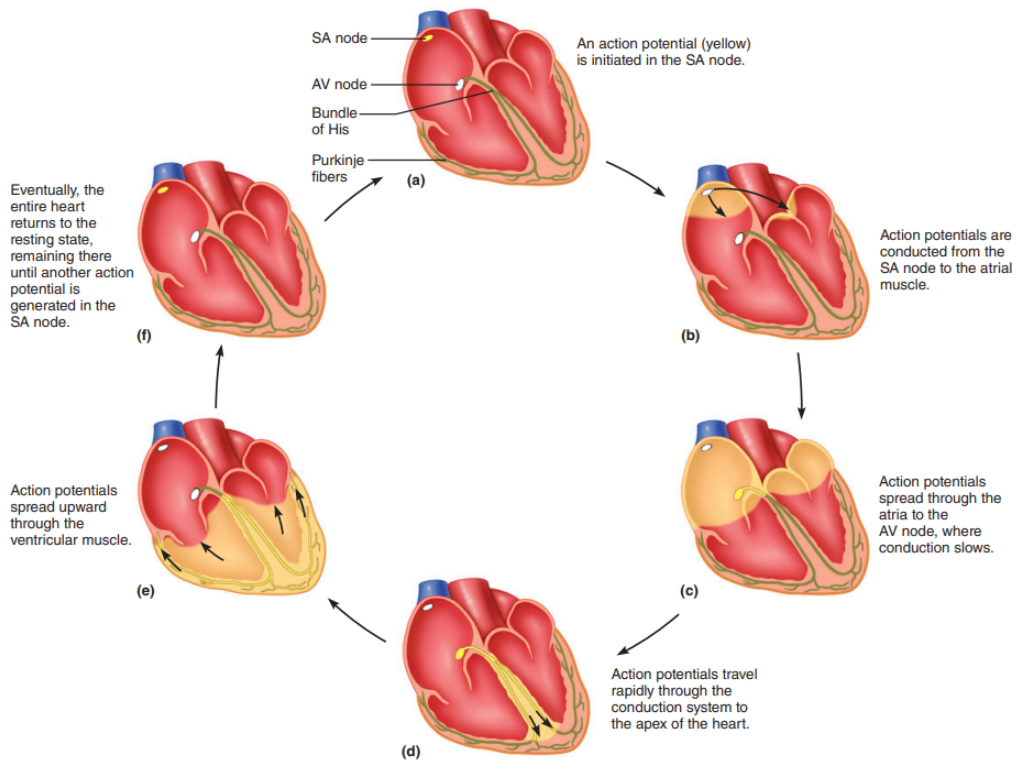


**Figure 2.6:** The spread of the action potentials through the heart [11].

## Electrocardiogram (ECG)

The electrocardiogram (ECG) represents an electrical tracing of the heart (Figure 2.9) and is recorded non-invasively by means of electrodes placed on the body surface. It is used as a diagnostic test to evaluate the electrical activity of the heart and the presence of anomalies.

The standard ECG procedure is based on an imaginary equilateral triangle surrounding the heart. This triangle is extended so that its corners correspond to the right arm, left arm, and left leg, forming a configuration known as Einthoven's triangle. Electrodes placed at the triangle's corners are connected in pairs to a device that measures voltage, such as an oscilloscope or recorder. These electrode pairs are called bipolar leads and are labeled with Roman numerals. Leads I, II, and III measure the potential difference between two limb electrodes: Lead I records the difference between the left and right arms, Lead II measures the difference between the left leg and the right arm, and Lead III measures the difference between the left leg and the left arm (see Figure 2.7).

The unipolar leads aVR, aVF and aVL were originally constructed by Goldberger

and they are derived by measuring the electrical potential at a single electrode, relative to the average potential of the other limb electrodes. These augmented leads provide unique perspectives on the heart's electrical activity, especially in relation to its vertical axis.

The limb leads, of which there are six (I, II, III, aVR, aVL and aVF) have the exploring electrode and the reference point placed in the frontal plane. These leads are therefore excellent for detecting vectors travelling in the frontal plane.

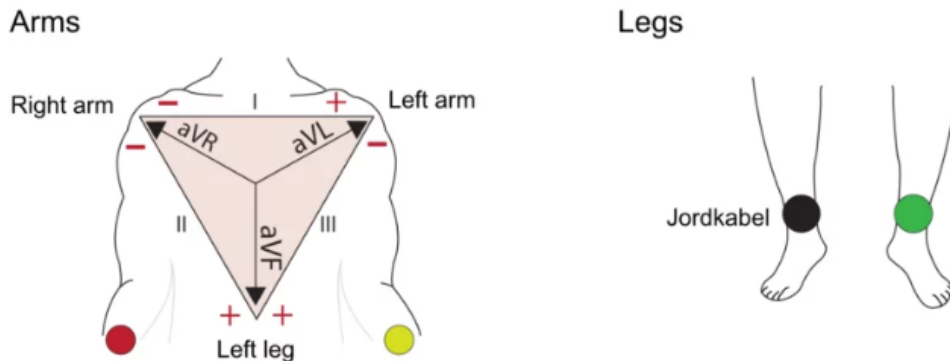


**Figure 2.7:** Einthoven's triangle and Goldberger's leads [13].

Clinical ECGs use chest electrodes as well as the limb electrodes, providing 12 different leads. This expanded setup offers a more detailed and complete view of the heart's electrical activity from different angles and perspectives. The 12 leads are categorized into two groups: the limb leads and the precordial (chest) leads.

The chest electrodes provide a horizontal view of the heart's electrical activity, complementing the vertical perspective of the limb leads. These leads allow for a more precise localization of electrical disorders within the heart, particularly in relation to the heart's anterior, posterior, and lateral walls. The anatomical placement of the chest leads electrodes is shown in Figure 2.8.

- Lead V1 is placed at the 4th intercostal space to the right of the sternum, providing information about the right side of the heart and the septum.
- Lead V2 is placed at the 4th intercostal space to the left of the sternum, continuing to assess the septum.
- Leads V3 to V6 move progressively along the chest, from the anterior to the lateral areas of the left ventricle, providing a detailed view of the electrical activity in the left side of the heart.

The ECG normally shows three characteristic waveforms:

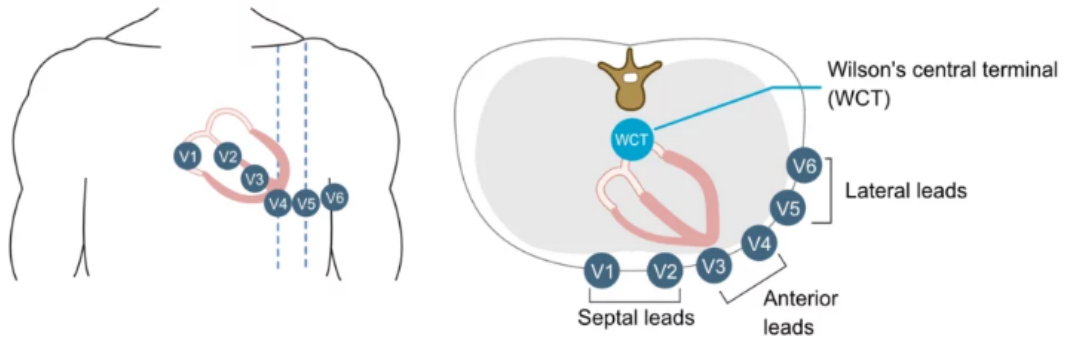


**Figure 2.8:** Anatomical placement of precordial leads [13].

1. The P wave is an upward deflection that is due to atrial depolarization;
2. The QRS complex is a series of sharp upward and downward deflections due to ventricular depolarization;
3. The T wave is an upward deflection caused by ventricular repolarization, correlated with phase 3 of the ventricular contractile cell action potential.

Atrial repolarization is generally not detected in an ECG recording because it occurs at the same time as the QRS complex. Between the waves, a normal ECG trace consists of a horizontal line, called the isoelectric line, indicating that no changes in electrical activity are occurring.

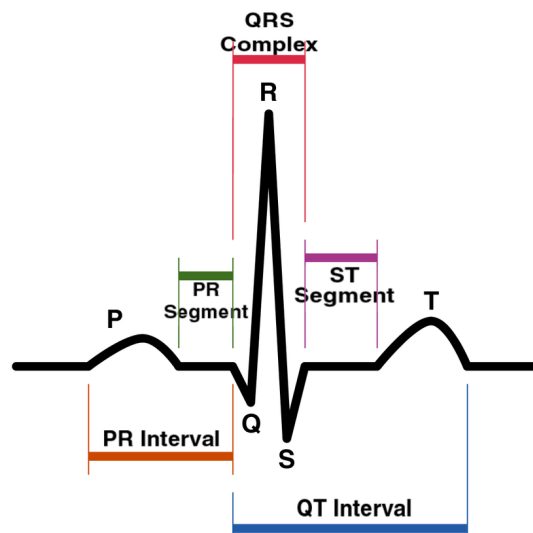


**Figure 2.9:** Electrocardiogram recording [14].

## Cardiac cycle

The cardiac cycle is a series of events that occur in conjunction with the flow of blood through the heart chambers during a single heartbeat. A single cardiac cycle is defined as a complete sequence of cardiac contraction (systole) and relaxation (diastole). An examination of the cardiac cycle may begin in the middle of diastole (Phase 1 in Figure 2.10), when both the atria and ventricles are fully relaxed and blood flows back to the heart via the systemic and pulmonary veins.

During this phase, the AV valves are open, thereby facilitating the flow of blood from the atria to the ventricles. Conversely, the pulmonary and aortic valves are closed due to the fact that the ventricular pressure is lower than that observed in the aorta and pulmonary arteries. At the conclusion of diastole, atrial depolarization, as indicated by the P wave on an electrocardiogram (ECG), initiates muscle contraction, propelling the remaining 20–30 % of ventricular filling. The duration of atrial systole is approximately 100 ms, concluding prior to the onset of ventricular systole as the atrial muscle returns to diastole.

Subsequently, the isovolumetric contraction phase succeeds the ventricular depolarization and is indicated by the QRS complex in the ECG. The onset of ventricular systole, which lasts for a total of 270 ms, is accompanied by the premature closure of the AV valves, which is triggered by the elevation of pressure within the ventricles. However, this is insufficient to prompt the opening of the semilunar valves. At this stage, there is no blood flow into or out of the chambers, as all the valves are closed. Consequently, the volume of blood within the ventricles remains constant. The isovolumetric contraction (Phase 2 in Figure 2.10) concludes when the ventricular pressure is greater than the pressures in the pulmonary trunk and the aorta, thereby enabling blood to exit the heart.

In the second phase of ventricular systole (Phase 3 in Figure 2.10), blood is ejected into the aorta and pulmonary arteries, resulting in the opening of the pulmonary and aortic valves. The pressure generated by the left ventricle will be significantly greater than that generated by the right ventricle, given that the existing pressure in the aorta will be considerably higher. The ventricular pressure reaches a peak and subsequently declines. When the pressure falls below that of the aorta, the semilunar valves close, marking the end of ventricular ejection. The quantity of blood pumped by one ventricle is referred to as the stroke volume. In the event that this is lower than the end-diastolic volume, it can be inferred that there is still blood remaining in the ventricle following contraction.

Immediately following the relaxation of the ventricles following repolarisation, as indicated by the T wave of the ECG, phase 4 is initiated (see Figure 2.10) and lasts approximately 430 ms. At this point, the pressure within the chamber drops below that of the pulmonary trunk and aorta. This results in blood flowing back towards

the heart, producing the dicrotic notch observed in blood pressure tracings. The semilunar valves are designed to prevent backflow into the heart. The closure of all valves maintains a constant volume of blood, which results in the first phase of ventricular diastole being referred to as isovolumetric relaxation. Once the pressure within the ventricles is lower than that of the atria, the tricuspid and mitral valves are prompted to open, allowing for the flow of blood from the major veins into the relaxed atria and subsequently into the ventricles. This marks the completion of the cardiac cycle [11].

### 2.1.2 Blood vessels

Blood circulates through the body in a closed-loop system, originating from the heart and subsequently reaching the tissues before ultimately returning to the heart. As blood exits the heart, the blood vessels divide and branch repeatedly, becoming more numerous and narrower in diameter. Capillaries, being the smallest blood vessels, are the site of exchange between blood and interstitial fluid. Subsequent to passing through these capillaries, the blood returns to the heart via vessels that gradually converge and increase in size as they become fewer in number.

Upon exiting the heart, blood is transported to the body's organs and tissues via relatively large vessels known as arteries. These arteries undergo repeated branching within the organs and tissues. The smallest arteries then divide into even smaller vessels called arterioles, which deliver blood to the capillaries.

Subsequent to passing through the capillaries, blood flows into larger vessels known as venules, which then connect to even larger vessels called veins. These veins then transport the blood back to the heart.

The circulation of blood through any vessel or network of vessels is governed by the relationship between the pressure gradient and the resistance of the vessel or network. This relationship can be summarised by Equation 2.1:

$$Q = \frac{\Delta P}{R} \quad (2.1)$$

where  $Q$  is the flow rate, which represents the volume of fluid the volume of blood moving through the vessel or network per unit of time;  $\Delta P$  is the pressure difference (or gradient) between two points along the vessel or network, which drives the blood flow;  $R$  is the vascular resistance, which is the opposition to blood flow.

The resistance experienced by blood flow is determined by the characteristics of the vessel in question. This resistance is influenced by various factors, including the diameter of the vessel, the viscosity of the blood, and the length of the vessel. The relationship between these factors was modelled using Poiseuille's law, which demonstrates that resistance is inversely proportional to the fourth power of the

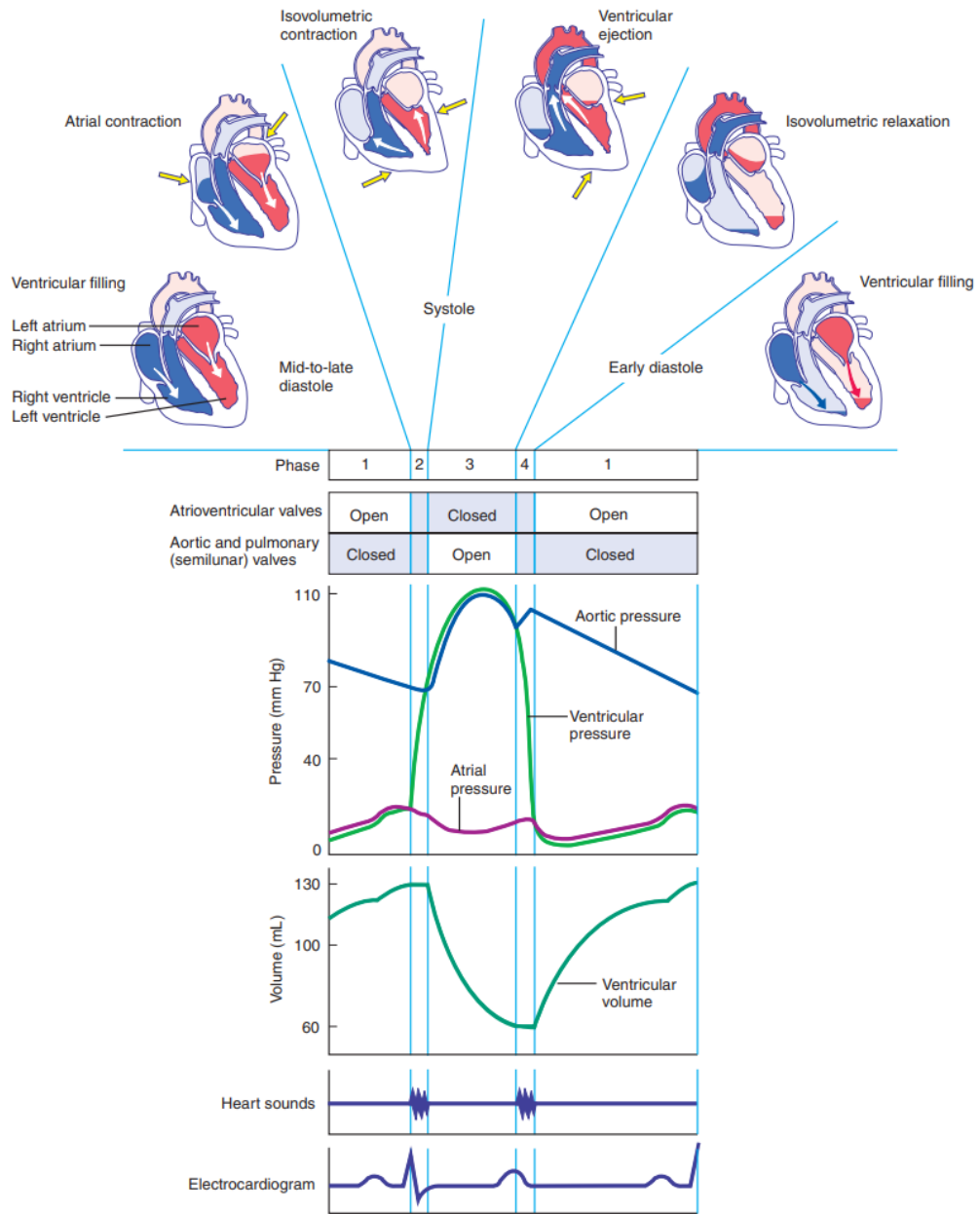


**Figure 2.10:** Illustration of cardiac cycle, the given values are referred to the left heart. It is possible to observe the relationship between changes in pressure gradient across the valves and the state of the valves themselves (open or closed), as well as the changes in the volume of the ventricles. Heart sounds are linked to the valves closing, while ECG waves are connected to the heart's mechanical actions [11].

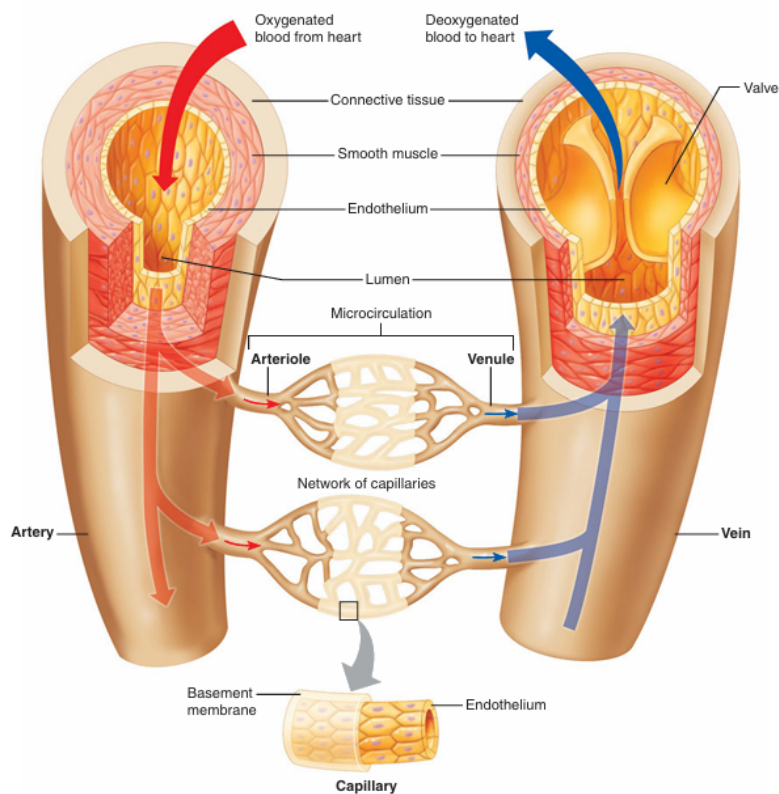


**Figure 2.11:** Blood vessels type [11].

vessel radius, how could be appreciate in Equation 2.2, where  $R$  is the resistance,  $\eta$  is the viscosity,  $L$  is the length, and  $r$  is the radius of the vessel. This indicates that as the radius increases, resistance decreases significantly. A decrease in blood vessel radius is known as vasoconstriction, while an increase in vessel radius is known as vasodilation.

$$R = \frac{8\eta L}{\pi r^4} \quad (2.2)$$

**Arteries** carry blood away from the heart, in particular the pulmonary arteries transport deoxygenated blood from the right ventricle to the lungs, while systemic arteries transport blood with a high oxygen concentration to the body tissues. The wall of an artery contains three layers as shown in Figure 2.11:

- The innermost layer consists of squamous epithelium surrounded by connective tissue basement membrane with elastic fibers.
- The middle layer is the thickest layer made up of smooth muscle cells.

- The outermost layer consists of connective tissue.

Arteries function as pressure reservoirs, the combination of thickness and elastic tissue gives them both stiffness and the ability to expand and contract with each heartbeat. During systole, the arteries stretch as blood is pumped in, thereby storing elastic energy. Conversely, during diastole, the arterial walls recoil, thereby propelling blood forward. This process is crucial for ensuring uninterrupted blood flow, even during periods when the heart is not actively pumping. Although blood flow is continuous, palpitation of arteries, such as the radial artery in the wrist, reveals a pulse. The pulse is caused by a pressure wave that travels along the arteries in response to blood being pushed into the arteries during systole, causing the arterial walls to expand. Arteries possess low compliance, which means that minor increments in blood volume result in substantial pressure changes, enabling them to efficiently store and release elastic energy (see Figure 2.12) [11].

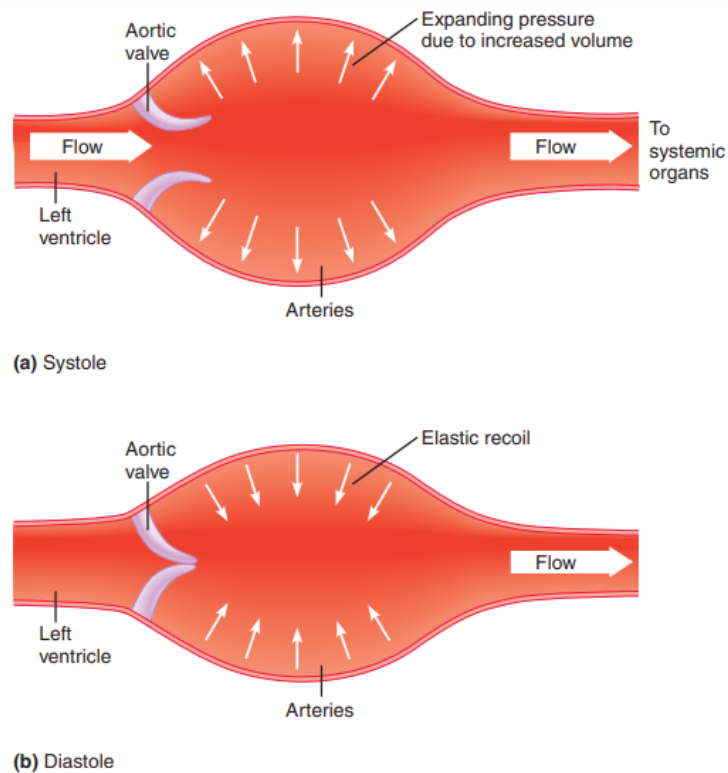


**Figure 2.12:** The role of arteries as a pressure reservoir [11].

**Arterioles** are small arteries that give rise directly to the capillaries. The walls of arterioles have minimal elastic material but are rich in circular smooth muscle, which surrounds the vessels. This smooth muscle exhibits the capacity

for contraction and relaxation, thereby modulating the diameter of the arterioles. Consequently, the arterioles play a pivotal role in the regulation of blood flow and, by extension, the volume of blood that enters the capillary beds. When the smooth muscle in the arterioles relaxes, blood flows into the capillaries, filling the entire bed. Conversely, when the smooth muscle contracts, blood flow to the capillaries is reduced, limiting blood supply to that area. It is also important to note that blood pressure drops sharply at the arteriole-capillary junction. This drop in pressure is crucial for enabling the exchange of materials between the blood and tissues within the capillary beds. The diameter of the arterioles is subject to intrinsic regulation in response to fluctuations in metabolic activity, blood flow, stretch of arteriolar smooth muscle (Myogenic Response), and locally secreted chemical messengers. The arteriolar radius is also subject to regulation by the sympathetic nervous system, which innervates the smooth muscle of the majority of arterioles. Hormones such as vasopressin and angiotensin-II represent an additional extrinsic factor that contributes to the regulation of arteriolar resistance through the induction of vasoconstriction.

**Capillaries** are the smallest blood vessels, with a diameter that is similar to that of a red blood cell. The structure of their walls consists of a single layer of endothelial cells, with a basement membrane situated beneath. This small diameter and thin structure facilitate the exchange of substances between blood and surrounding tissues. Because of their extensive branching, the total cross-sectional area of capillaries is considerably greater than that of the other blood vessels. The substantial number of capillaries in the human body, estimated to range between 10 and 40 billion, creates a surface area for exchange of around 600 square metres.

**Venules** are small vessels formed by the merging of capillaries. They are slightly smaller than arterioles, with thinner walls and little to no smooth muscle. Smaller venules resemble capillaries, having a porous endothelial layer that allows exchange between blood and interstitial fluid.

**Veins** collect blood from venules and have slightly larger diameters than arteries, with walls that are thinner due to the significantly lower blood pressure within veins in comparison to arteries. Despite their thinner walls, the structural composition of venous walls are very similar to that of arteries. Veins feature of one-way valves, which are crucial for the unidirectional flow of blood towards the heart, thereby preventing backflow into the organs and tissues. Unlike arteries, which function as pressure reservoirs, veins function as volume reservoirs, exhibiting greater compliance than arteries. A relatively small increase in the pressure within veins results in a substantial expansion (increase in volume). Thus veins can contain greater quantities of blood than arteries, despite the significantly lower pressure within veins [11].

### 2.1.3 Blood

Blood is a precious body fluid that carries oxygen and nutrients to living cells and removes their waste products. It also provides immune cells to fight infection and contains platelets, which play a vital role in wound healing. Each year in the USA, 30 million units of blood components are transfused to patients who need them. The total volume of blood in an average healthy adult is 5.5 L. It consists mainly of plasma and erythrocytes, but also includes leukocytes and platelets. The elements of the blood are separated according to their density by centrifuging a blood sample. The fraction of erythrocytes in the blood is defined as the hematocrit, which is a useful clinical index of normal blood composition. It depends on many factors such as gender, but also the normal adaptive response in low-oxygen environments [11].

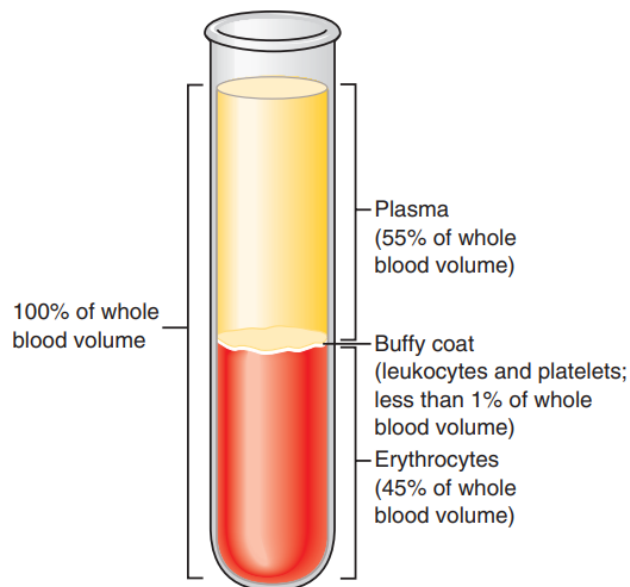


**Figure 2.13:** Following centrifugation, a blood sample is obtained for composition analysis [11].

#### Plasma

Plasma constitutes the aqueous solution that comprises over 55% of blood's total composition (see Figure 2.13). It is essential for the components of blood to circulate throughout the entire body. Its composition is distinguished by the presence of a diverse variety of solutes, including proteins, small nutrients, gases, metabolic waste products and electrolytes.

## Erythrocytes

Erythrocytes, also known as red blood cells, are the most prevalent type of cell in the blood. Their function is transporting oxygen and carbon dioxide throughout the body. Erythrocytes are nucleated cells, in other words they are characterized by the absence of a nucleus. Their plasmatic membrane is able to deform and flex in order to navigate capillaries, which can be of a diameter smaller than the cells themselves. This flexibility is attributed to the presence of a cytosolic protein called spectrin. They have a biconcave disk shape that gives them a large surface area, which is fundamental for the exchange of respiratory gases.

The main function of erythrocytes is to take up oxygen from the lungs and transport it to the body's tissues, and to carry carbon dioxide from the tissues to the lungs. Their ability to transport respiratory gases is due to the presence of two proteins in their cytoplasm: haemoglobin and carbonic anhydrase.

Hemoglobin is the most abundant protein in erythrocytes, it is composed of four polypeptide chains, each of which contains a ring-shaped iron-containing molecular component known as heme group (see Figure 2.14). This iron gives erythrocytes their red colour and is the site where oxygen binds reversibly to hemoglobin. It is evident that, due to the presence of four heme groups within each hemoglobin molecule, a maximum of four oxygen atoms can be bound per hemoglobin.

Carbonic anhydrase is an enzyme that catalyses the reversible conversion of carbon dioxide and water to carbonic acid. It is fundamental in the transport of carbonic carbon dioxide only [15].

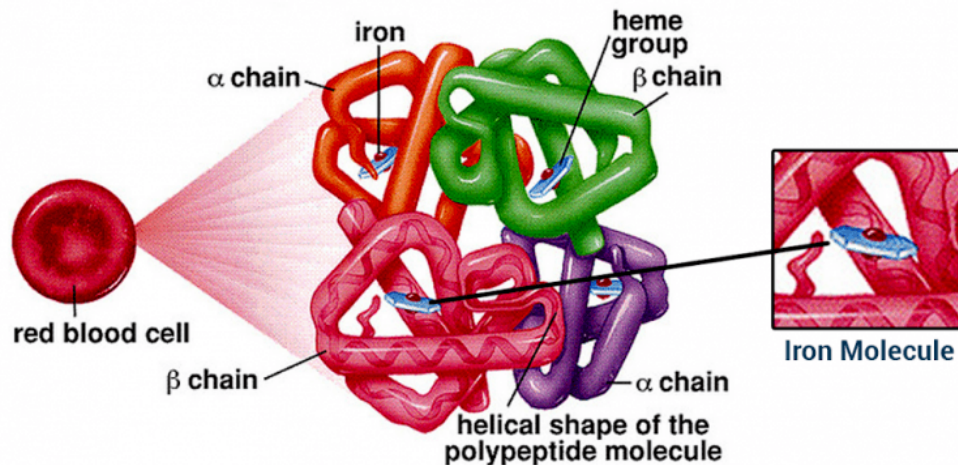


Figure 2.14: Hemoglobin [15].

## Leukocytes

Leukocytes, otherwise referred to as white blood cells, are crucial components of the immune system which are present in the blood in comparatively low numbers when compared to erythrocytes. These cells are able to circulate both within the blood and other bodily tissues, and upon encountering injury or illness, they have the capacity to attack any external microorganisms or other foreign materials that enter the body. They are categorized into five main families of leukocytes, each of which plays a distinct role in the immune system. These types are: neutrophils, eosinophils, basophils, monocytes and lymphocytes.

**Neutrophils** are the most abundant white blood cells and they are the first to get involve in cases of bacterial infections. They perform phagocytosis, engulfing and digesting pathogens.

**Lymphocytes** include three different families: B cells, T cells, and natural killer (NK) cells. The first group produce antibodies, while T cells help regulate immune responses and attack infected cells. Instead NK cells are responsible to target and destroy tumor or virus-infected cells.

**Monocytes** are large cells that circulate in the blood and migrate to tissues, where they mature into macrophages and dendritic cells. They can perform phagocytosis and promote the activation of other immune cells.

**Eosinophils** defend the body against parasitic infections releasing enzymes and toxins. They modulate allergic responses and help control inflammation.

**Basophils** operate by releasing toxic molecules that damage invaders. Furthermore, they secrete chemical mediators such as histamine, which play a substantial role in the occurrence of allergic reactions and inflammation.

## Platelets

Platelets are small, colorless cell fragments that form when portions of large bone marrow cells called megakaryocytes break off. They are smaller than red blood cells and contain mitochondria, smooth endoplasmic reticulum, and cytoplasmic granules, but no nucleus. These cells are vital for initiating the process of blood clot formation that is essential to stop the bleeding. These mechanisms occurs in three steps: vascular spasm, formation of a platelet plug, and formation of a blood clot, or thrombus.

## 2.2 Cardiovascular diseases

Cardiovascular diseases (CVDs) are a group of diseases of the heart and blood vessels that represent the leading cause of death on a global scale. According to the World Health Organization, 17.9 million people died from CVDs in 2019, corresponding to 32% of all global deaths [1].

Of these death, the majority is caused by ischemic heart disease that involves the reduction of blood flow to the heart muscle. CVDs also include: ischemic stroke, incerebral hemorrhage, rheumatic heart disease, hypertensive heart disease, cardiomyopathy and myocarditis, atrial fibrillation and flutter, and other other less prevalent conditions. The number of CVD deaths steadily increased from 12.1 million in 1990, reaching 18.6 million in 2019 and reflecting the population growth and aging (see Figure 2.15).

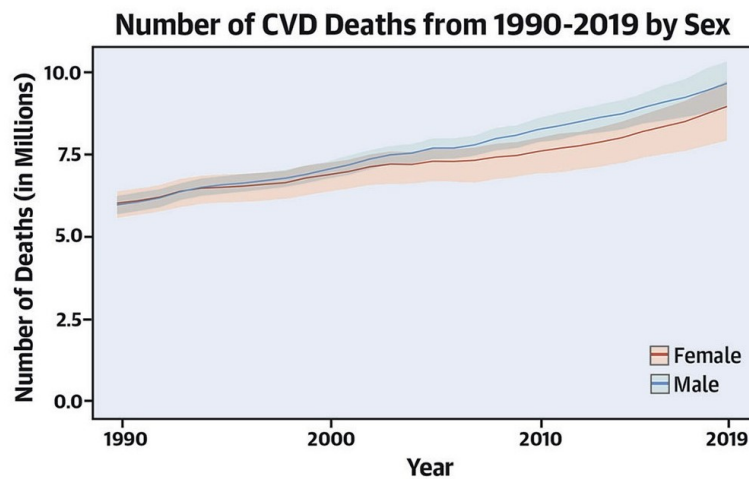


**Figure 2.15:** Number of CVD Deaths from 1990-2019 by Sex [3].

It is estimated that at least 75% of global deaths from cardiovascular diseases (CVDs) occur in low- and middle-income countries. In these regions, there is often a lack of access to primary healthcare programmes that are essential for the early detection and management of individuals with risk factors for CVDs [1].

The primary cause of a heart attack is atherosclerosis that is a chronic inflammatory disease of the arteries. It is principally a process driven by lipids, initiated by the accumulation of low-density lipoprotein (LDL) and remnant lipoprotein particles and an active inflammatory process in focal areas of arteries particularly at regions of disturbed non-laminar flow at branch points in the arteries.

Atherosclerosis is a predominantly asymptomatic condition until narrowing of the vessel lumen or thrombus precipitation obstruct blood flow to the heart

(coronary heart disease), brain (ischemic stroke), or lower extremities (peripheral vascular disease). The most common of these symptoms is coronary heart disease, including stable angina pectoris and the acute coronary syndromes. Some medical conditions must be considered as warning signals including hypercholesterolemia (LDL-cholesterol), hypertension, diabetes mellitus and high blood triglycerides. The most significant behavioural risk factors are unhealthy diet, physical inactivity, tobacco use and harmful use of alcohol. The risk of atherosclerosis increases also with age and a family history of premature heart disease [4].

The lesion development is triggered by the presence of adaptive intimal thickening in specific regions of the arterial tree, characterized by smooth muscle cell accumulation within the intima. As these macrophages consume the LDL cholesterol, they transform into foam cells, which contribute to the growth of atherosclerotic plaques. Initially, foam cells accumulate within the proteoglycan layer of the intima, and once multiple layers have formed, they become visible to the naked eye as yellow-colored xanthomas or fatty streaks. While many xanthomas do not progress further, some, particularly in areas prone to atherosclerosis, develop into progressive lesions. Small lipid pools form beneath the foam cell layers without significant disruption to the normal structure of the intima. This type of lesion is known as pathological intimal thickening, commonly observed in coronary arteries between the ages of 20 and 30. In some cases, lipid pools expand into confluent necrotic cores (also referred to as lipid-rich cores) due to macrophage invasion. This disrupts the normal structure of the intima, leaving behind a mass of lipids and cell debris called a fibroatheroma. Over time, the necrotic core and surrounding tissue may become calcified, resulting in a fibrocalcific plaque. Plaque rupture is the most common cause of thrombosis. In this event, a defect in the fibrous cap exposes the thrombogenic core to the bloodstream. Dislodged plaque material is often found within the thrombus, indicating that rupture and thrombosis occurred simultaneously, reinforcing their causal relationship (see Figure 2.16).

### 2.2.1 Hypertension and Arterial stiffness

Arterial stiffness is the resistance offered by the arterial wall to deformation, due to loss of elasticity. Although wall stiffness cannot be measured directly *in vivo*, indices of arterial stiffness can be obtained through:

- the assessment of the relation between changes in arterial pressure and variations in arterial volume, cross-sectional area, or diameter;
- the evaluation of Pulse Wave Velocity (PWV), a functional parameter influenced by arterial wall stiffness.

One of the most common used indices of arterial stiffness is the volume compliance

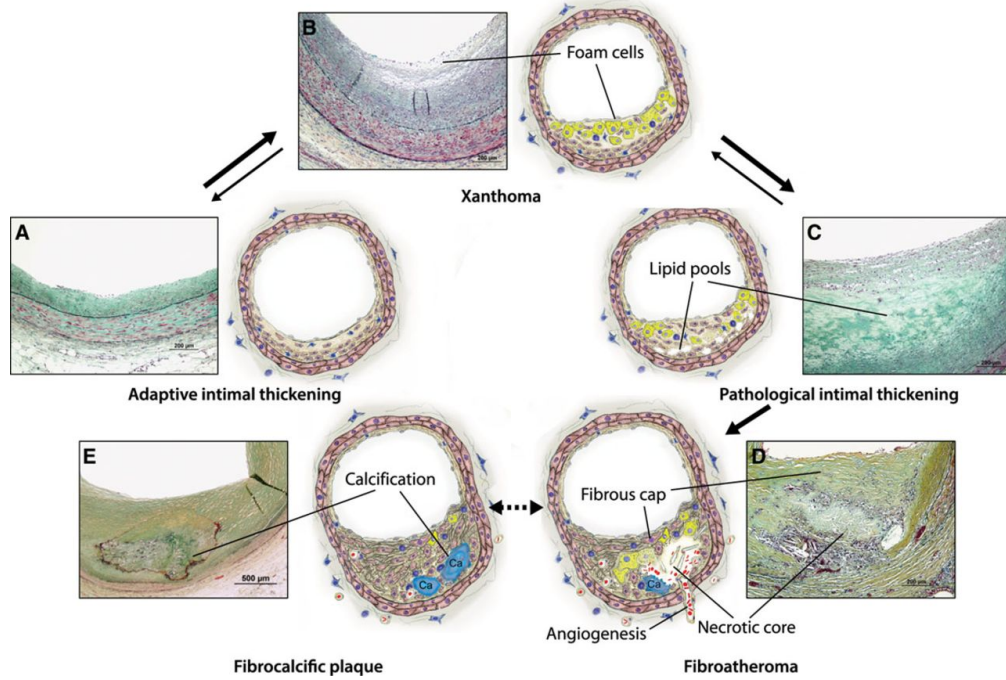


**Figure 2.16:** Lesion types of atherosclerosis [16].

that is measure of arterial distensibility that is expressed by Equation 2.3. It mostly depends on arterial intrinsic elastic properties, and is a determinant of the propagation speed of the pulse pressure wave. Compliance is defined as the ratio between change in arterial volume and change in arterial pressure:

$$Compliance = \frac{\Delta V}{\Delta P} \quad (2.3)$$

Systemic conduit arteries typically play a crucial role in cushioning blood flow, ensuring a steady flow in the microvasculature despite the intermittent ejection of blood from the Left Ventricle (LV) as previously stated. However, when large arteries become stiff (Large-Artery Stiffening, or LAS), this cushioning function is compromised, leading to several negative consequences that significantly impact cardiovascular health.

First, LAS contributes to isolated systolic hypertension, a prevalent condition linked to a large portion of global cardiovascular morbidity and mortality. This condition is characterized by elevated systolic blood pressure with normal or low diastolic pressure, leading to an increased pulse pressure. Second, LAS reduces coronary perfusion pressure and raises LV afterload, which can lead to LV remodeling, dysfunction, and failure, even without the presence of coronary artery disease.

Third, LAS exacerbates the penetration of pulsatile energy into the microcirculation of target organs, particularly those with high blood flow demands and low arteriolar resistance.

Interestingly, while arterial-wall stiffening precedes isolated systolic hypertension and directly contributes to target organ damage, the arterial wall itself is also a target organ, heavily affected by aging and various pathological conditions such as diabetes, obesity, smoking, hypercholesterolemia, and Chronic Kidney Disease (CKD). As a result, LAS plays a central role in a harmful cycle of hemodynamic dysfunction, marked by excessive pulsatility, ultimately contributing to Heart Failure (HF), impaired coronary perfusion, cerebrovascular disease, and other chronic health issues. Reflecting the crucial role of arterial stiffness in cardiovascular function, LAS measurement are strong indicators of future cardiovascular events [17].

## 2.3 Pulse Wave Velocity

The PWV is defined as the velocity of the pressure wave generated by blood ejection from the heart, propagates along the arterial wall thanks to the distensibility of the arteries. PWV has emerged as a critical biomarker of cardiovascular health. Alterations in PWV indicate changes in arterial function because of its intrinsic link to the elasticity of the arterial vessels. Pulse wave travels more slowly in younger with healthier and more elastic vessels. In comparison, increased arterial stiffness leads to faster pulse wave propagation, resulting in a higher PWV [18].

### 2.3.1 Pulse Wave

The heart's contraction generates a pressure variation within the arteries, which subsequently propagates through the vascular system as a pulsating wave. When the heart ejects blood, it raises blood pressure and stretches the aortic wall, creating a wave of compression and distension that travels along the aorta and other large arteries. As systole comes to an end, the reduced rate of cardiac ejection causes a relaxation wave, leading to a drop in pressure and a decrease in the aortic diameter [19].

The pulse waveform is the sum of the forward pressure wave generated by the heart contraction and the reflected pressure waves that resulted from wave terminations in the peripheral arterial trees (see Figure 2.17). Increased central arterial stiffness is associated with a high-amplitude forward wave and a higher PWV, determining a faster forward and backward (reflected) wave speeds. The earlier arrival of wave reflections to the aorta causes a variation of physiological wave shape, with a progressive loss of diastolic pressure augmentation and an

increase in late systolic augmentation. Beyond the commonly measured values of systolic, diastolic, and mean arterial pressure, additional clinically relevant insights regarding vascular age can be obtained by analyzing the morphology of pulse wave signals [17].

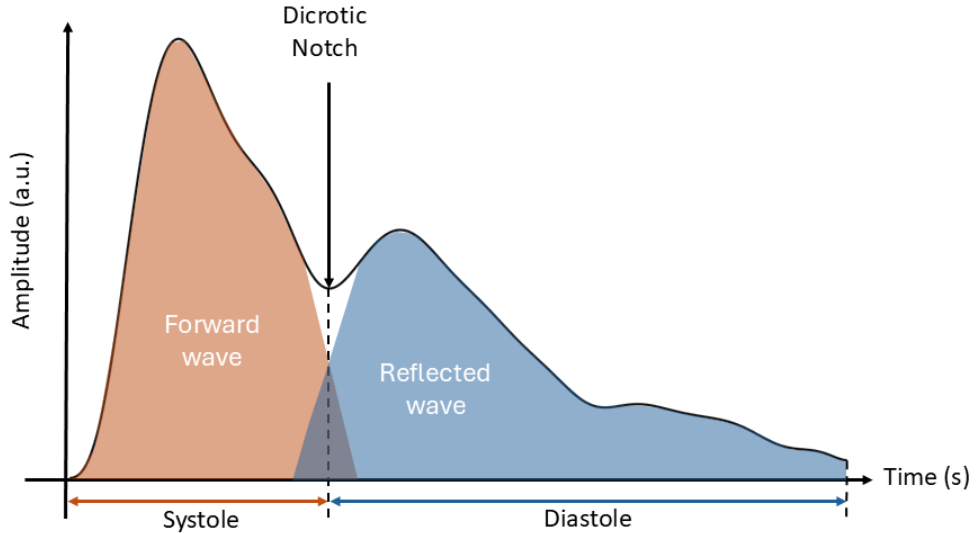


**Figure 2.17:** Carotid pulse waveform.

### 2.3.2 PWV estimation

The PWV can be measured along various paths within the human body. The carotid-femoral path reflects the artery stiffness of the central arteries, specially the aorta, which is a key indicator of cardiovascular risk. The relative PWV is measured between the carotid artery in the neck and the femoral artery in the groin. Carotid–femoral PWV (cf-PWV) is measured non-invasively by tonometry with the foot to foot method, which represents the gold standard. The foot of the curve corresponds to the end-diastole point as identified by the intersecting tangent point method (see Figure 2.17) [20].

That method requires to record two pressure waves at the carotid and femoral arteries (Figure 2.18), the carotid-femoral PWV (*cfPWV*) is calculated by dividing traveled distance ( $D$ ) by pulse transit time (*cfPTT*) as can be seen in in Equation 2.4.

$$PWV = \frac{D}{cfPTT} \quad (2.4)$$

The large majority of devices quite accurately measure transit time as the time

delay between the arrival of the pulse wave at the common carotid artery ( $hcPTT$ ) and the common femoral artery ( $hfPTT$ ) as formulated in Equation 2.5.

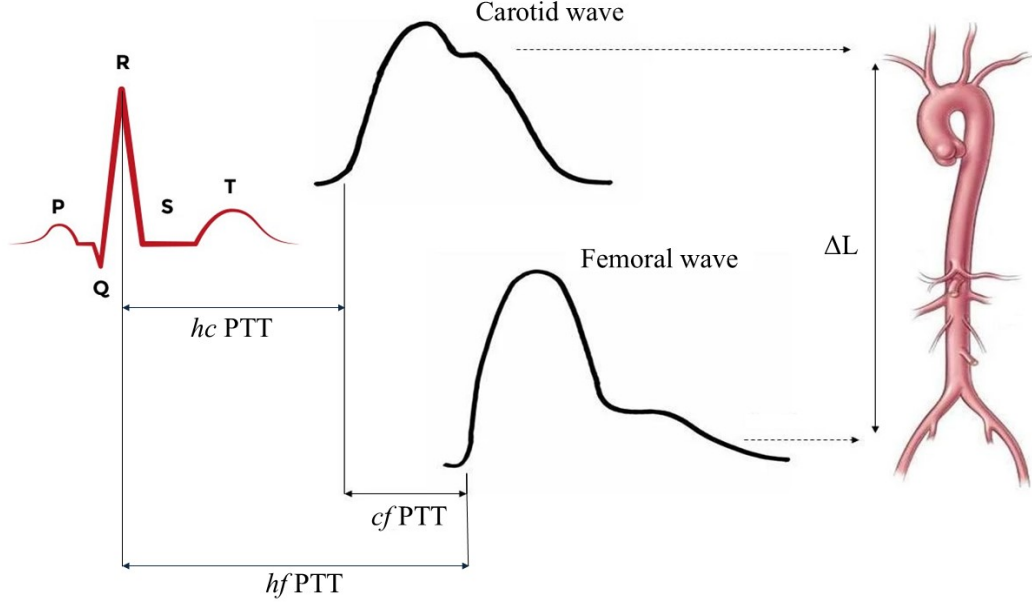


**Figure 2.18:** Carotid-femoral Pulse Transit Time estimation.

$$cfPTT = hfPTT - hcPTT \quad (2.5)$$

In literature, different measurement of distance  $D$  can be found. Of all currently used distances the 80% of the direct carotid-femoral distance  $\Delta L$  appeared the most accurate, only slightly overestimating the real traveled distance by 0.4% [21]. The direct distance between the arterial points is usually measured in a straight line, with a flexible meter and then it's multiplied by the corrective factor as in Equation 2.6.

$$PWV = 0.8 * \frac{\Delta L}{cfPTT} \quad (2.6)$$

Since the compliance or distensibility of the vessel  $C$  can be characterized in terms of the changes in cross-sectional area  $A$  and pressure  $P$  (Equation 2.8), the relationship between arterial distensibility and PWV can be express by the Bramwell-Hill equation (Equation 2.7).

$$PWV = \sqrt{\frac{A \Delta P}{\rho \Delta A}} = \sqrt{\frac{1}{C \rho}} \quad (2.7)$$

where:

- $A$  is the mean area of the blood vessel;
- $\Delta P$  is the difference between the central systolic and diastolic pressures;
- $\rho$  represents the density of the blood, it is considered constant;
- $\Delta A$  is the difference between the maximum and minimum area of the blood vessel during a cardiac cycle;
- $C$  is the compliance of the vessel, defined as follow:

$$C = \frac{\Delta A}{A\Delta P} \quad (2.8)$$

The pulse wave velocity is inversely proportional with the root square of distensibility. Consequently, even minor changes in the stiffness of the arterial walls can have a considerable impact on the speed of the pulse wave, which is critical for assessing cardiovascular health [20].

### 2.3.3 Clinical devices for PWV estimation

Different measurement techniques have been developed to determine non-invasively the PWV, they can perform regional or local measurements of arterial stiffness. Regional PWV assessment is typically performed on two different arteries, commonly the carotid and femoral arteries. Typical pulse assessment sites include areas where the pulse is easily felt, such as the radial, common carotid, brachial, or femoral arteries. However, regional PWV provides only the average PWV over a long segment composed of arteries with different mechanical properties, which means it may mask local variations in arterial properties and doesn't provide information on specific arterial abnormalities or localized biomechanical features. Furthermore, the distance measurement between the test points, based on external methods, is often inaccurate and can be problematic, particularly in cases of tortuous vessels, which are not accounted for in external distance estimation. Local PWV measurement is clinically important for analyzing the biomechanical properties of the arterial wall at specific sites. Arterial mechanical characteristics vary along the arterial tree and are differently influenced by aging and disease. In the early stages of atherosclerosis, elastic properties are locally altered, making local PWV assessment valuable for diagnosing changes in large arteries [5].

Ultra Sound (US) and Magnetic Resonance Imaging (MRI) are two imaging technique used to estimate the local PWV of a arterial segment. MRI determines the PWV by capturing high-resolution images of the arterial walls and blood flow. The technique involves using phase-contrast MRI, which visualizes and quantifies the blood flow speed through the arteries. To calculate PWV, the distance  $\Delta d$  is

measured along the length of the vessel in the image (represented by the dashed line in Figure 2.19A, while the temporal shift is determined using the time-to-peak (TTP) method between the flow waveforms in the two defined transverse planes. MRI systems are constrained by their high costs and the need for specialized infrastructure and trained staff, limiting their availability to well-equipped clinical centers and research institutions. Additionally, MRI examinations are more time-consuming than other PWV measurement techniques [22].

The US technique allows the determination of the PWV by estimating the time delay between the diameter waveforms recorded simultaneously at two close positions along the vessels, leveraging the Doppler effect as in Figure 2.19B. In some cases the devices analyze the waves separately using ECG synchronization. These techniques depend on a reliable identification of the foot of the diameter waveforms and a sufficiently high sampling frequency [5].

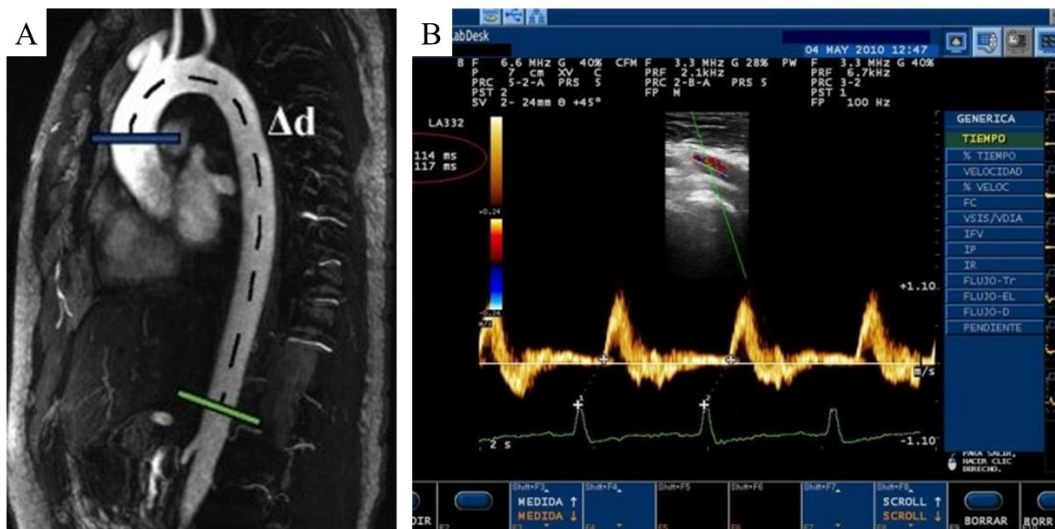


**Figure 2.19:** PWV measurements based on imaging technique. A) MRI at the aortic arch [22] ; B) US at femoral artery synchronized with ECG [23].

Electromechanical devices are considered the gold standard method for measuring the PWV. This method provides accurate and reliable regional assessments of arterial stiffness.

*SphygmoCor*<sup>®</sup> (AtCor Medical, Sydney, Australia) is widely regarded as the clinical gold standard for PWV estimation, employing an integrated electrocardiogram (ECG) unit and a tonometric sensor mounted to a pen-like support (Figure 2.20).

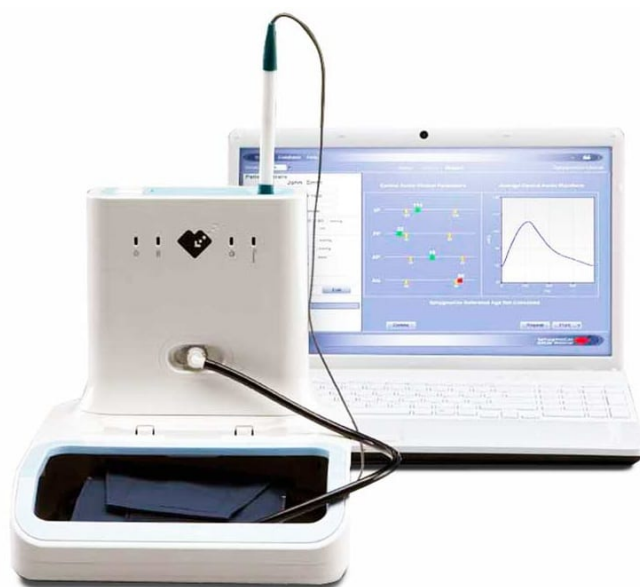


**Figure 2.20:** Illustration of the SphygmoCor device [24].

The tonometer functions by delicately flattening (or applanating) the artery at specific points, such as the carotid and femoral arteries, utilizing a pressure sensor. Synchronization of this measurement with the R-wave of the ECG (which corresponds to the electrical activation of the heart) enables the device to calculate the time delay between the arrival of the pulse at each site. This time difference, combined with the known distance between the measurement points, is used to determine the pulse wave velocity.

*PulsePen*<sup>®</sup> (DiaTecne, Milano, Italy) is equipped with a wireless receiver, an ECG unit (given that pulse wave registration is not simultaneous), and high-definition tonometry (Figure 2.21). Since 2014, a version with two tonometers has been available, allowing for PWV evaluation without the need for an ECG.



**Figure 2.21:** Illustration of the PulsePen device [25].

*Complior Analyse*<sup>®</sup> (Alam Medical, Paris, France) features two piezoelectric mechanical transducers that allow for the simultaneous acquisition of two pulse waves from carotid and femoral sites (Figure 2.22). The device provides additional probes for radial and distal measurements. This setup enables simultaneous PWV evaluation across three distinct segments, facilitating the assessment of the stiffness of peripheral arteries.



**Figure 2.22:** Illustration of the Complior Analyse device [26].

The *Arteriograph*<sup>®</sup> system is equipped with an inflatable cuff that is placed on the patient's upper arm and inflated to 45 mmHg above the individual's systolic blood pressure. Pressure variations are detected by a pressure sensor, and the signal is transmitted to a computer. The acquisition of PWV is based on the generation of two systolic peaks: the first peak (P1) represents the systolic volume ejection in the aorta, while the second, smaller peak (P2) corresponds to the reflected wave pressure from peripheral arteries. The return time (RT) is the difference between the first peak (P1) and the reflected systolic peak (P2). PWV is then calculated using the formula in the Figure 2.23.

The *Athos* system is an experimental device developed by the eLiONS research group in Politecnico di Torino for noninvasive pulse wave velocity evaluation. It is made up of two pen-shaped probes (see Figure 2.24), each of which is equipped with a high-precision MEMS force sensor at the tip. These ergonomic probes are positioned on two distinct locations on the subject's body: distal (femoral or wrist) and proximal (carotid) arterial sites [28]. The two probes, composed of a dedicated PCB and a rechargeable battery, will send their data thanks to bluetooth low energy connection, to the base station. The base station, connected to a laptop via USB acts as a data collector for the data streaming as well as a charging station for the two probes. The two pulse waves are shown real-time on a GUI exploiting

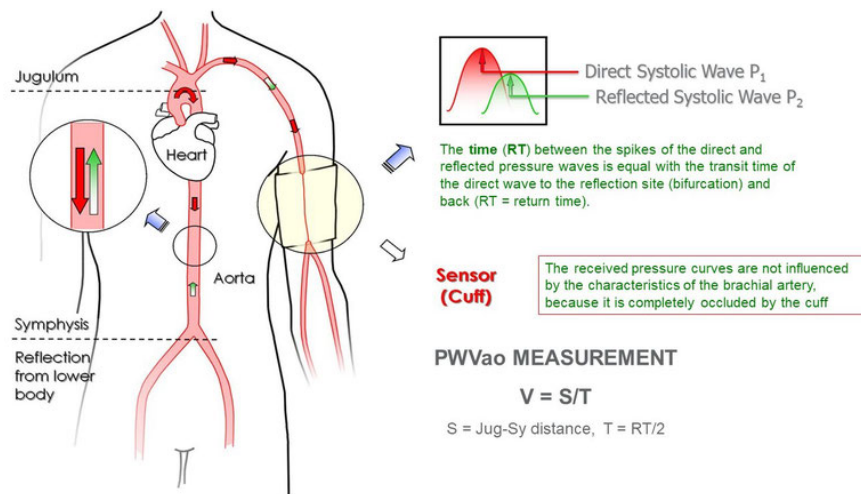


**Figure 2.23:** Illustration of the Arteriograph device [27].

the intersecting tangent point algorithm to determine the PWV parameter. As soon as they leave the base station, the two probes are electronically synchronized, ensuring the measurement's accuracy [29].

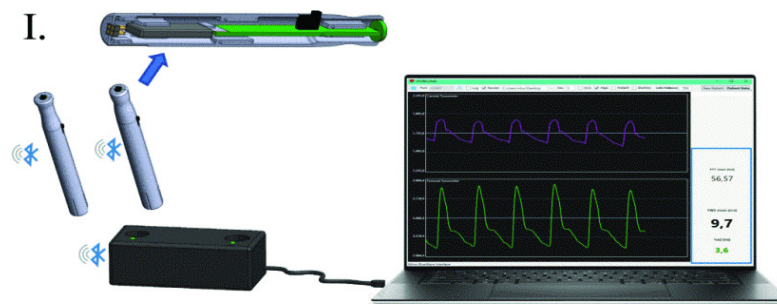


**Figure 2.24:** ATHOS system overview and details of the probe [29].

The electromechanical devices are sensitive to variations in the pressure applied to the arteries or to the angle between the artery and the sensor, so the currently technology is operator-dependent. The use of these devices requires a certain level of skill, which can impact the accuracy of measurements. Consequently, the tonometry-based PWV assessment technique is primarily employed in research and clinical settings by trained operators, but it is not widely used in routine clinical or ambulatory environments. Additionally, patient-related factors, such as obesity, can present challenges. These conditions may hinder proper sensor placement or signal acquisition, affecting the reliability of PWV measurements. A major

challenge is to develop new instrumental solutions that allow for more accurate PWV assessment with fewer approximations and relatively low-cost techniques, making them suitable for use in everyday clinical practice [5].

The Impedance Plethysmography (IPG) technique is a simple, non-invasive and a low-cost method. This technology results a promising candidate as an alternative to current clinical methods. Furthermore, the instrumentation and electronics required for IPG measurement enable the development of a miniaturised device. Another advantage of the IPG is the possibility to observe a pulse in every artery, despite the depth of the artery [30].

## 2.4 Impedance Plethysmography

Impedance plethysmography (IPG) is a non-invasive and continuous method for detecting changes in the conductivity of the measurement target caused by changes in the absolute and relative volumes of the tissues with different conductivities. The IPG signal mainly originates from the changes in the volume of blood in the arteries. A pressure pulse causes the diameter of an artery to change, which in turn affects the amount of blood in that artery. When the blood volume in the artery increases, the conductivity of the tissue in that area also increases, leading to a decrease in impedance. The changes in bioimpedance are mainly due to the conductivity of blood being greater than that of other tissues [7].

The arterial vessel can be modeled as an elastic cylindrical tube, its impedance is directly affected by the cross-sectional area  $A$  as in Equation 2.9,

$$Z = \frac{\rho L}{A} \quad (2.9)$$

where  $L$  represents the length of the measured segment and  $\rho$  is the tissue resistivity. The IPG measurement provides the impedance value of a body segment that is regarded as the parallel model of the blood and tissue (Figure 2.25). The resulting impedance is expressed by the Equation 2.10.

$$\frac{1}{Z} = \frac{1}{Z_a} + \frac{1}{Z_b} \quad (2.10)$$

where  $Z_a$  and  $Z_b$  are the impedance of the artery and tissue respectively. Because of the tissue impedance is assumed to remain constant from Equation 2.9 and Equation 2.10, the change in arterial cross-sectional area  $\Delta A$  can be expressed as a function of the change in measured impedance  $\Delta Z$  (Equation 2.11).

$$\Delta A \approx \frac{\rho_b L \Delta Z}{Z_b^2} \quad (2.11)$$

in which  $\rho_b$  is the resistivity of blood and  $Z_b$  represents the basal impedance of the segment.

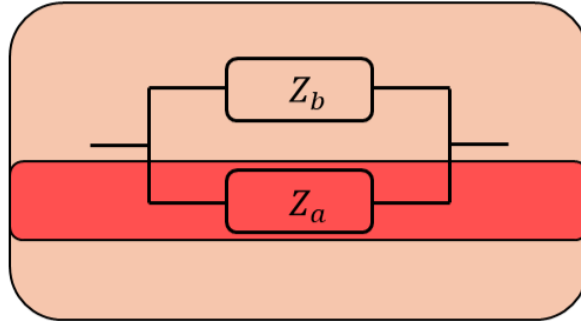


**Figure 2.25:** Impedance model of the blood and its surrounding tissue.

The bioimpedance measurement is performed using an array of four electrodes placed along the vessel or transversally (see Figure 2.26). The outer (excitation) electrodes inject a fixed alternating current (AC), and the inner (sensing) electrodes perform the acquisition of a voltage signal proportional to the instantaneous impedance of tissues. In this way the impedance can be computed using the Equation 2.12,

$$Z = \frac{V}{I} \quad (2.12)$$

where  $V$  is the voltage and  $I$  is the current injected.

As long as the impedance measurement is conducted at an adequate sampling rate, the heart rate component will be detectable in the signals. In this setup, the signal envelope consists of a pulsatile component  $Z(t)$  that reflects cardiac activity, and a static component  $Z_0$  representing the average impedance of the tissues (see Figure 2.27). However, to extract the impedance variations, the acquired waveform needs to be demodulated. A key challenge in impedance plethysmography is accurately detecting very small impedance changes of only a few  $\text{m}\Omega$  within a signal that spans several orders of magnitude in  $\Omega$ .

The sensitivity of the technique is found to be significantly influenced by the distance between the electrodes and the frequency of the injected current. It has been demonstrated that increasing the interelectrode distance (IED) results in a deeper current distribution within the tissues. Furthermore, an analogous effect is observed when the frequency of the applied AC current is increased [31, 32]. In impedance plethysmography, frequencies typically used fall within the range of 10 kHz to 100 kHz, with current injection levels below one milliamper, which is

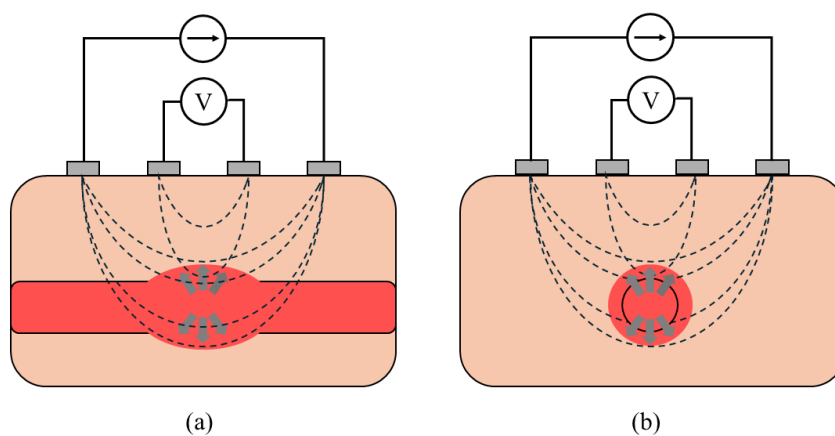


**Figure 2.26:** Electrodes placement for IPG acquisition. Outer (excitation) electrodes inject current and inner (sensing) electrodes measure the voltage. (a) Parallel and (b) Transversal configuration.

in compliance with the IEC60601-1. According to Anderson [33], blood exhibits higher conductivity compared to other tissues like muscle and fat in this frequency range.

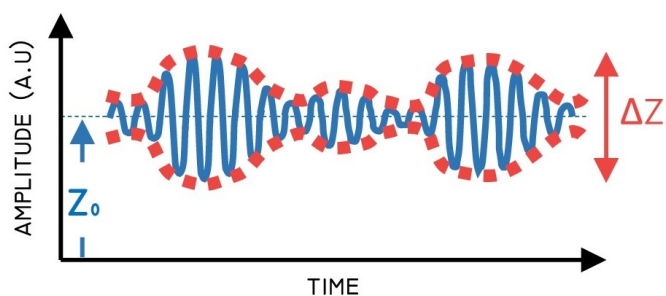


**Figure 2.27:** IPG waveform [34].

### 2.4.1 IPG application to PWV estimation: a state of the art

The potential of impedance plethysmography for assessing vascular health has led to numerous feasibility studies aimed at evaluating the accuracy and practicality of the technique in clinical settings. For example, Huynh and Jafari proposed a model for non-invasive cuff-less blood pressure estimation and PTT detection based on a photoplethysmography sensor and IPG. The first sensor was attached to the index finger to measure the PTT while the IPG sensor was placed on the wrist at different locations to measure the signal quality in which the sensor was moved each 1 cm horizontally and each 2 cm vertically. The research has revealed that using impedance magnitude to estimate PTT offers promise to realize wearable and cuffless BP devices [8].

Wiegerinck et al. conducted a pilot study to explore whether IPG could be a suitable technique for measuring pulse wave velocity in the legs as an alternative to the tonometer method. They used the intersect tangents method to estimate the pulse arrival time, which helps in identifying fiducial points. The PWV estimates obtained from bioimpedance measurements are generally consistent with those derived from the tonometer [9].

The study by Wang et al. [10], investigated how the placement of electrodes affects the resolution of IPG measurements. To identify an optimal electrode arrangement for high-resolution IPG measurement, they evaluated various distances between excitation and sensing electrodes. A longer interval could reduce current density in the artery region due to current amplitude loss caused by the isotropic path. Conversely, a shorter distance between the excitation electrodes might lead to lower current in the artery region, as it results in a shallower through-depth due to the narrow spacing. Additionally, the study assessed the impact of different excitation frequencies on impedance measurements.

# Chapter 3

## Materials

This chapter outlines the materials used in the development of the device. First, a detailed overview of the impedance measurement system is provided, followed by a description of the devices used for the hardware design and in vivo validation tests.

### 3.1 Impedance measurement system

Bioimpedance measurements require the injection of a known low-level current into the patient. A schematic representation of the IPG hardware is provided in the Figure 3.1, it comprises a current generator, which was developed with a monopolar Improved Howland current pump. This converter transforms the applied voltage into a fixed AC current, which is then delivered to the tissues through an external electrode pair.

In accordance with the findings of analogous studies, the amplitude of the injected current was found to be in the hundreds of  $\mu\text{A}$ , with a frequency of 50 kHz [35, 8]. It was demonstrated that this frequency resulted in a greater impedance change between systolic and diastolic blood pressure [10].

The analog input (AI) of the NiDAQ USB-6259 is used to acquire the voltage drop across the sensing electrode pair, which defines the measurement segment. Simultaneously, the analog output (AO) generates a sine-wave voltage that is fed into the Howland current pump to control the current injection. The configuration of the NiDAQ USB-6259 was conducted through the utilization of the MATLAB<sup>®</sup> software interface by means of a USB connection.

For the purpose of current injection and voltage signal acquisition, Ag/AgCl electrodes are used, each with a diameter of 24 mm and equipped with conductive and adhesive hydrogel for enhanced contact quality. The Kendall<sup>™</sup>H124SG electrodes from CardinalHealth<sup>™</sup> and ECG cables used are shown in Figure 3.2.

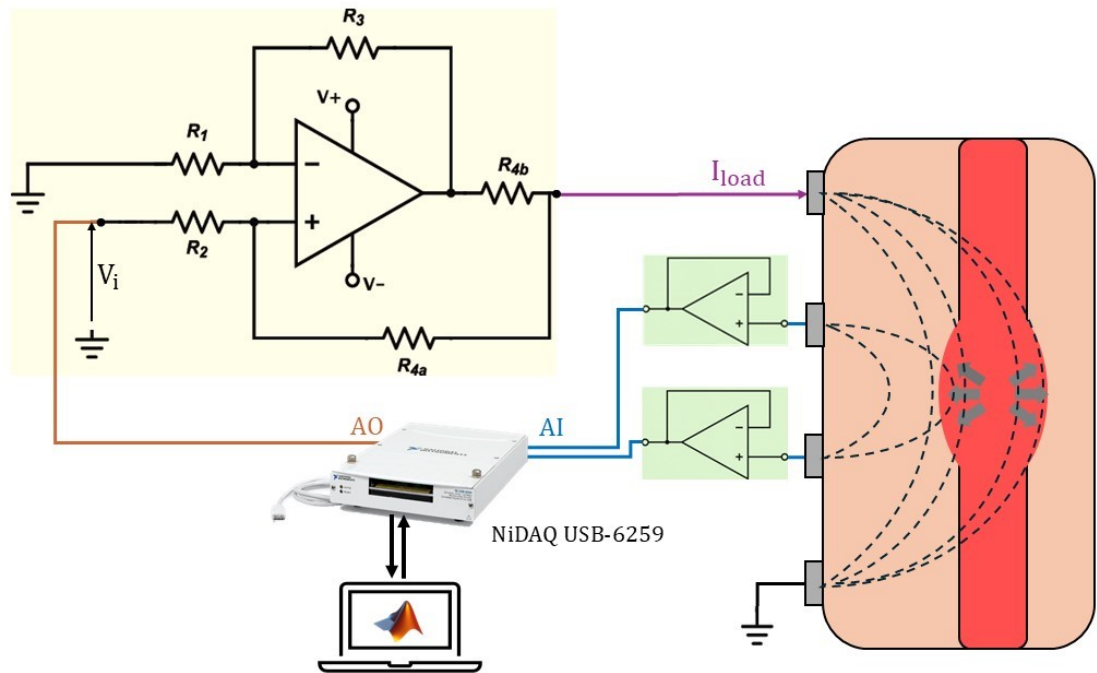


**Figure 3.1:** Impedance measurement system. The yellow box represents the Howland current pump, which acts as a voltage-controlled current source, injecting a constant alternating current into the tissues. The NiDAQ USB-6259 then acquires the voltage signal between the inner electrodes, which is generated by the current flow through the tissue and its impedance. The voltage followers, depicted in the green box, are placed between the electrodes and the ADC to ensure signal integrity by preventing loading effects and minimizing distortion.

To ensure signal stability during transmission and minimize attenuation due to the long cables connecting the electrodes to the acquisition board, two voltage followers were placed as close as possible to the electrodes. These voltage followers offer the advantages of high input impedance and low output impedance. The high input impedance of the voltage follower ensures minimal interaction with the preceding circuit, drawing almost no current from the signal source. As a result, the loading effect is avoided, meaning that the performance of the previous circuit remains unaffected by the connection to the ADC. This configuration enhances the fidelity and accuracy of the measurements by maintaining signal integrity throughout the transmission path. The following paragraphs will provide a comprehensive description of each component of the impedance measurement system and the rationale behind the project's selection.



**Figure 3.2:** Standard pre-gelled and self-adhesive disposable electrodes and ECG cables.

### 3.1.1 Howland Current Pump

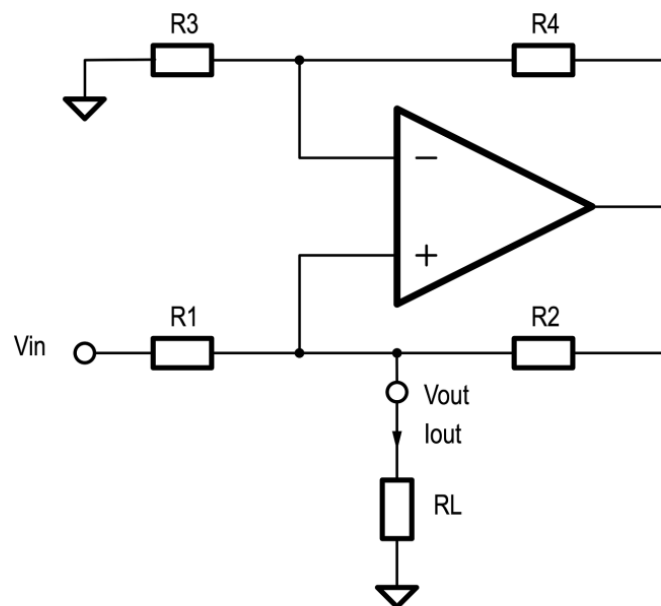


**Figure 3.3:** Basic Howland Current Pump.

The Howland Current Pump (HCP) is a circuit that uses a difference amplifier to impose a voltage across a shunt resistor, creating a voltage-controlled current source capable of driving a wide range of load resistances. Several feasibility

studies in the literature highlight the potential of using the HCP for impedance measurements, demonstrating its ability to provide stable, controlled currents necessary for accurate impedance characterization across various components and systems [8, 35].

The core of the Howland Current Pump is an op-amp, which is used to maintain feedback that controls the output current to match the desired value. The current is determined by the voltage applied at the non-inverting input of the op-amp and the values of the resistors in the loop (Equation 3.2). The circuit will adjust to supply the appropriate current through the load, irrespective of the load's resistance (within limits). The independence of the circuit from the load resistance is demonstrated in the subsequent lines.

The basic configuration of the Howland Current Pump is illustrated in the Figure 3.3, the current flowing through the load resistor is the sum of the currents through the resistors  $R_1$  and  $R_2$  (Equation 3.1).

$$I_{out} = \frac{V_{in} - V_{out}}{R_1} + \frac{V_{out}(1 + \frac{R_4}{R_3}) - V_{out}}{R_2} \quad (3.1)$$

The output current can be formulated as in the Equation 3.2.

$$I_{out} = \frac{V_{in}}{R_1} + \frac{V_{out}}{R_o} \text{ where } R_o = \frac{R_2}{\frac{R_4}{R_3} - \frac{R_2}{R_1}} \quad (3.2)$$

In the Equation 3.2  $R_o$  is effectively the output impedance of the circuit as seen from the output node. The impedance of the output node is observed to tend towards infinity when a matched resistor ratio is set. This results in the output acting as a voltage-controlled current source with a specific value stated by the Equation 3.3.

$$\frac{R_4}{R_3} = \frac{R_2}{R_1} \rightarrow I_{out} = \frac{V_{in}}{R_1} \quad (3.3)$$

The application note published by National Instruments [36] highlights the critical importance of resistor matching and precision in this context. In a Howland Current Pump, the utilization of resistors with a high tolerance can result in substantial deviations, particularly in the output impedance, which can have a significant impact on performance, particularly in precision applications. In order to achieve optimal precision, it is often preferable to employ resistors with tight tolerances, thereby ensuring the necessary current accuracy and stability. While precision resistors can incur higher costs, they are often the preferred option when compared to the use of a trim pot, which necessitates additional trimming and

carries the risk of mis-trimming and instability over time. This ensures the current source remains reliable and accurate, especially in critical applications.

Another significant factors that must be given due consideration are the amplifier Common-Mode Rejection Ratio (CMRR) and the finite gain band width product (GBWP), which have the capacity to compromise the output impedance. The final parameter is of particular significance in instances where the specific application demands the generation of alternating current at a specified frequency.

One of the main limitations of the Basic Howland Current Pump is its output capability. The output node typically does not swing close to the supply rails. With a 1:1 resistor ratio, the output voltage is limited to less than half of the op-amp's supply voltage. As the output voltage increases, the op-amp needs to raise its output voltage significantly to maintain the desired current, but it can only swing so far before hitting the supply rail. Once this limit is reached, the op-amp can no longer provide the required output, which results in a restricted current range. If the output node voltage increases significantly, the op-amp's output must rise about twice as high to maintain the current. When this becomes unachievable, the "Improved Howland Current Pump" should be considered (Figure 3.4).

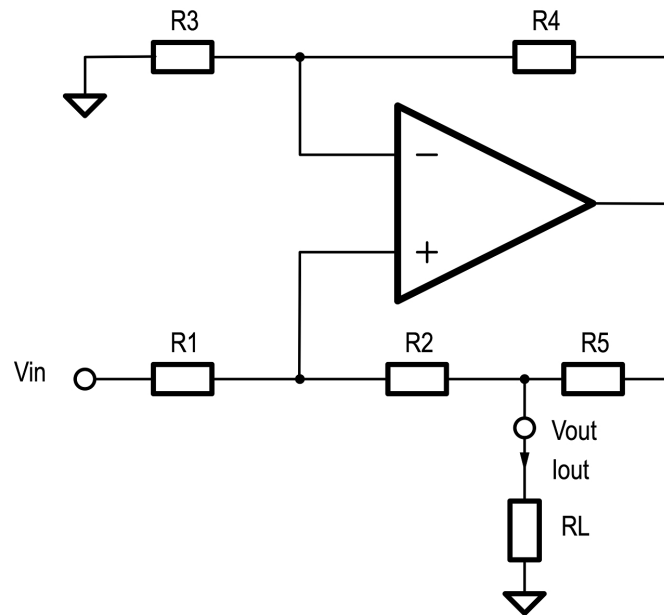


**Figure 3.4:** Improved Howland current pump.

In the Figure 3.4, the gain is set by  $R_5$  which can be placed at low values

and take advantage of a much greater output swing. The output current is now expressed by the Equation 3.4.

$$I_{out} = \frac{V_{in} \frac{R_4}{R_3}}{R_5} \quad (3.4)$$

In the Improved HCP, the resistor values must match as in Equation 3.5.

$$\frac{R_1}{R_2 + R_5} = \frac{R_4}{R_3} \quad (3.5)$$

The Howland current pump generally incorporates a small feedback capacitor positioned across the feedback resistor, with values ranging from 3 to 10 pF. In circumstances where a very slow current is being injected and the rate of change of the output voltage at the output node is not elevated, it has been demonstrated that increasing the value of the capacitor up to 1 nF can be advantageous. This adjustment has been shown to reduce both the bandwidth and the noise.

### 3.1.2 NiDAQ USB-6259

The NI 6259 is a multifunction I/O product of National Instruments' data acquisition systems (see Figure 3.5). It incorporates both analogue and digital input, as well as counter/timer functionality. The device features 16 differential or single-ended analogue input (AI) channels, with an ADC resolution of 16 bits and a maximum sampling rate of 1.25 MHz. The maximum working voltage is  $\pm 11$  V. In the context of multichannel operation, the aggregate maximum sampling rate is set at 1 MHz.



**Figure 3.5:** NiDAQ USB-6259

The number of analog output (AO) channels is four, with a maximum update rate of 2.86 MHz when operating in single-channel mode and an output range of  $\pm 10$  V. The AO waveform modes can be categorised as follows: non-periodic waveform, periodic waveform regeneration mode from onboard FIFO, and periodic waveform regeneration from host buffer including dynamic update [37].

The configuration of the acquisition board was facilitated by the utilization of the Data Acquisition Toolbox in Matlab®, a support package designed for National Instruments' devices. The toolbox applications enable the configuration and execution of a data acquisition session in an interactive manner. The data can be analyzed during its acquisition or stored for subsequent processing [38].

## 3.2 E4990A Impedance Analyzer

The E4990A Impedance Analyzer is a high-precision test instrument developed by Keysight Technologies for measuring the impedance of electronic components and materials across a wide frequency range. Its primary applications include circuit design, material testing, quality control, and R&D.



**Figure 3.6:** E4990A Impedance Analyzer Keysight Technologies [39].

Its functionality encompasses impedance measurement across a wide frequency spectrum from 20 Hz to 120 MHz. It offers a high level of measurement accuracy, with a basic impedance accuracy of  $\pm 0.08\%$  (typical  $\pm 0.045\%$ ). The analyzer supports a large impedance range from  $25\text{ m}\Omega$  to  $40\text{ M}\Omega$  and enables various measurement parameters such as impedance, resistance, reactance, capacitance, inductance, and more, including AC and DC voltages and currents.

Additionally, it features a built-in DC bias range from 0 V to  $\pm 40$  V and 0 A to  $\pm 100$  mA, making it suitable for testing components under controlled conditions. The enhanced measurement speed option has been developed to improve performance at higher frequencies, and the device includes a 10.4-inch color LCD touch screen that allows for 4-channel, 4-trace data display. The analyzer also supports data analysis functions such as equivalent circuit analysis and limit line tests, which are useful for both research and production environments [39].

### 3.3 Biosignalplux ECG

*biosignalplux* is a versatile platform designed for collecting and analyzing physiological data from wearable sensors. It supports multiple types of biosignal sensors, such as ECG, EMG, EEG, and more, allowing real-time, wireless data acquisition.

The platform is modular and customizable, enabling users to select the sensors they need for their specific applications. It offers high precision and sensitivity, ideal for research, healthcare, and sports performance monitoring. Due to its compact design, this professional biosignals kit can even be used for signal acquisition in dynamic conditions. The system includes OpenSignals software for data visualization and analysis and can integrate with cloud storage for remote access. With low power consumption and a compact design, it's suitable for a range of environments, including labs, clinics, and outdoor settings [40].



**Figure 3.7:** 8-Channel *biosignalplux* kit

In this project, the 8-Channel *biosignalplux* kit was used (Figure 3.7). This innovative device enables up to 10 h of signal streaming at a sampling rate of 3 kHz

and 16-bit resolution per channel, while simultaneously recording data from up to eight sensors.

The low-noise ECG sensor (Figure 3.8) uses a local differential triode configuration, allowing for fast and unobtrusive single-lead ECG data collection. The advanced design of the analog frontend is optimized for capturing intricate details in the ECG signals, ensuring high-quality, medical-grade raw data suitable for accurate analysis. This configuration is ideal for environments that require precise heart monitoring with minimal interference, such as in medical diagnostics, healthcare applications, and continuous heart health tracking [41].

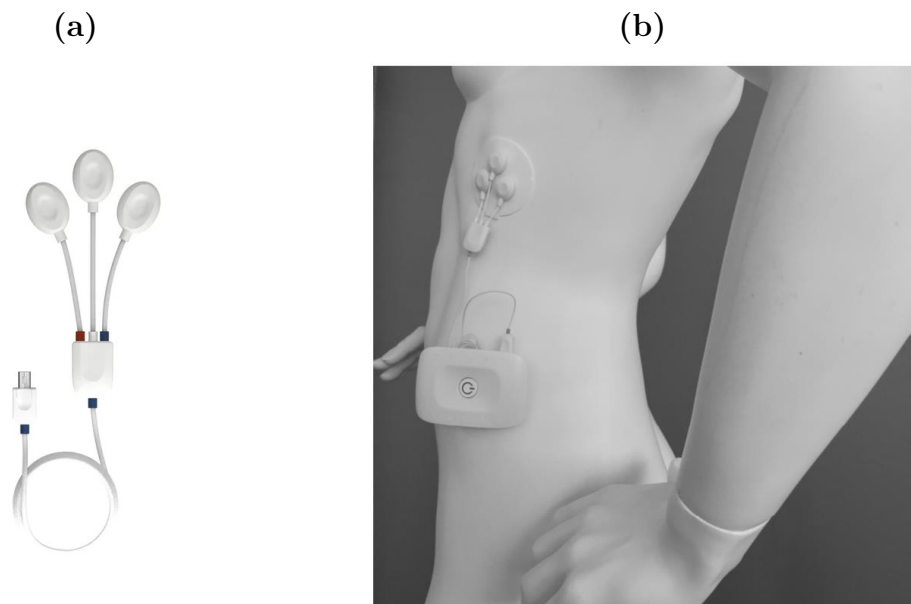


**Figure 3.8:** (a) Standard biosignalsplux ECG sensor with short electrode cables (4cm + 6cm + 4cm) and (b) example sensor placement using an ECG triod (equivalent to a standard medical-grade V6 lead) [41].

# Chapter 4

## Hardware Design

As previously mentioned (chapter 3), the Howland current pump is a key component of the impedance measurement system. Its primary function is to inject alternating current through the tissue. The high output impedance of the pump ensures a constant and stable current, enabling precise measurements of small variations in impedance. This stability is a crucial factor in ensuring the accuracy of impedance-based measurements.

### 4.1 Estimation of Load Impedance

To appropriately design each component of the voltage-controlled current source for the specific application, tissue impedance measurements were performed using the E4990A Impedance Analyzer described in chapter 3. In this manner, an accurate estimation of the load resistance was obtained.

#### 4.1.1 Methods and Results

Tissue impedance was assessed by placing the measurement electrodes on the wrist. Estimation was performed using four channels and the Keysight Kelvin probe set. This consists of two gold-plated flat tweezers with special gripping surfaces. This design ensures very precise contact with the component and very accurate measurements. The ground guard connector eliminates ground related errors. The gold plating helps to reduce the contact resistance between the surfaces of the probe and the lead of the component being measured - reducing overall error [42].

The contribution of the cables' impedance and the effect of different electrode dimensions were investigated. Furthermore, the electrodes were positioned at two distinct distances (12 cm and 5 cm) to assess the extent to which impedance

increases with increasing tissue volume length. Two different types of inspection were performed:

- frequency domain analysis within the range 20 kHz - 100 kHz that includes the measurement frequency of 50 kHz (chapter 3),
- fixed frequency of 50 kHz and variable current amplitude (1 mA, 10 mA, 20 mA).

First, the calibration of the E4990A Impedance Analyzer was executed as reported in technical specifications of the device [39]. Three calibration standards must be connected to the analyzer's test ports in the correct order. The analyzer will automatically guide the user through the calibration process:

- Open standard: a connector with no connection at the end.
- Short standard: a connector with the end short-circuited.
- Load standard: a connector with the end connected to a known impedance load, typically a precision resistor.

After each connection, the analyzer will adjust its internal calibration coefficients based on the reference measurements improving the measurement accuracy.

The results of the impedance measurement show what was expected: the tissue impedance decreases as the frequency of the applied current increases as shown in Figure 4.1. It is also clear that the impedance module is higher when the electrodes are placed further apart, as this increases the tissue volume between them.

At very low frequencies, the current cannot easily penetrate the cell membrane due to its high capacitance, meaning the impedance measurement primarily reflects the behavior of the extracellular fluid (ECF), as the membrane essentially acts as a barrier (Figure 4.2).

At very high frequencies, the capacitive effect of the cell membrane becomes negligible, allowing the current to flow freely through both the intracellular fluid (ICF) and extracellular fluid (ECF). In this case, the impedance measurement reflects the resistances of both the ICF and ECF [43].

As mentioned previously, a second type of impedance inspection was conducted by applying a current signal with varying amplitudes, while maintaining a fixed frequency of 50 kHz. The impedance of the tissue remained largely unchanged, being independent of the current amplitude. For an interelectrode distance (IED) of 12 cm, the impedance was approximately 740  $\Omega$ , whereas for an IED of 5 cm, it was around 680  $\Omega$ .

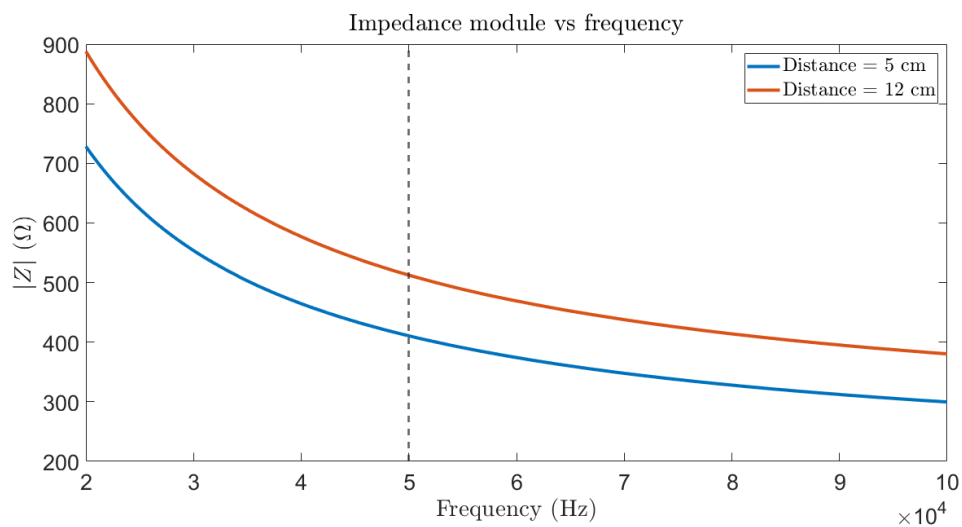


**Figure 4.1:** Frequency-dependent impedance trend for two different testing distances (5 cm, 12 cm), the dashed line indicates the frequency of the applied current signal.

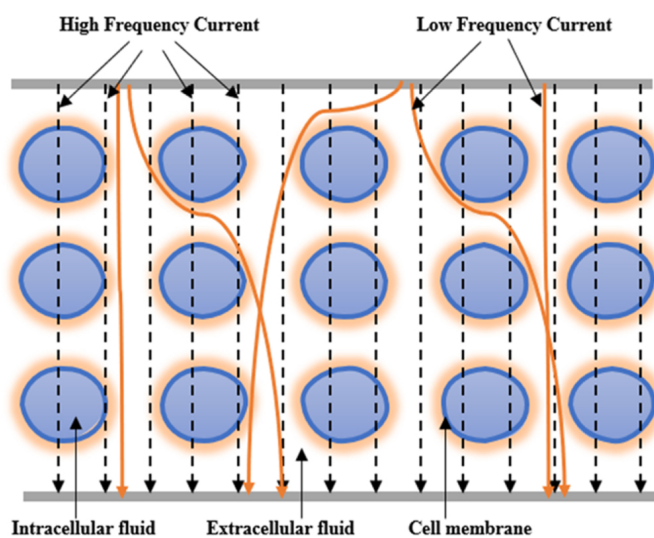


**Figure 4.2:** High and low frequency current distributions in cell suspensions [43].

The contribution of cables and contact impedance to the total impedance module was found to be less than  $500\ \Omega$ . This value was determined by calibrating the instrument with ECG cables and electrodes (Figure 3.2) connected to a Kelvin probe, followed by the connection of a standard reference to the electrode.

## 4.2 Howland current pump (HCP) design

Considering the results about the load impedance illustrated in the previous lines and technical specifications defined in the previous chapter the Improved Howland Current Pump was designed.

### Amplifier selection

The first stage of hardware development consisted of selecting the most suitable amplifier, chosen for its ability to handle the high rate of the input voltage waveform. The Gain-Bandwidth Product (GBWP) plays a critical role in the output impedance of the Howland Current Pump, as a low GBWP can lead to degradation of the output impedance.

For the reasons mentioned above, the LT1498, a Dual Rail-to-Rail Input and Output Precision C-Load Op Amp designed by Analog Devices, was selected. This amplifier delivers outstanding accuracy and stability with low offset voltage and minimal temperature drift, making it ideal for high-precision applications. Its rail-to-rail input and output capability allows it to handle signals that are very close to the supply rails, maximizing the usable output range. Additionally, the LT1498 is optimized to drive capacitive loads effectively, ensuring stable operation even in circuits with significant capacitive elements.

The amplifier offers a Gain-Bandwidth Product (GBWP) of 10 MHz, and while the Common-Mode Rejection Ratio (CMRR) is not linear at 50 kHz, it achieves approximately 85 dB when supplied at  $\pm 15$  V. The LT1498 is available in the standard dual op-amp configuration, housed in 8-pin PDIP and SO packages [44].

Following a rigorous evaluation process, a secondary amplifier was chosen for the designated application: the OPA2892, designed by Texas Instruments. This precision, low-noise operational amplifier is specifically engineered for high-performance applications. It offers a Gain-Bandwidth Product (GBWP) of 2 GHz and a wide supply voltage range of up to  $\pm 18$  V. Notably, it features two amplifiers in the same package, similar to the first amplifier [45].

### Resistors design

The resistance value was selected from the available options in the E12 series. To satisfy the condition outlined in Equation 3.5, the resistance  $R_4$  is implemented using a series combination of two resistors, as listed in the Table 4.1 along with the others.

This configuration ensures an optimal output current of approximately 495  $\mu$ A when a 5 V input voltage signal is applied. The signal amplitude was selected to

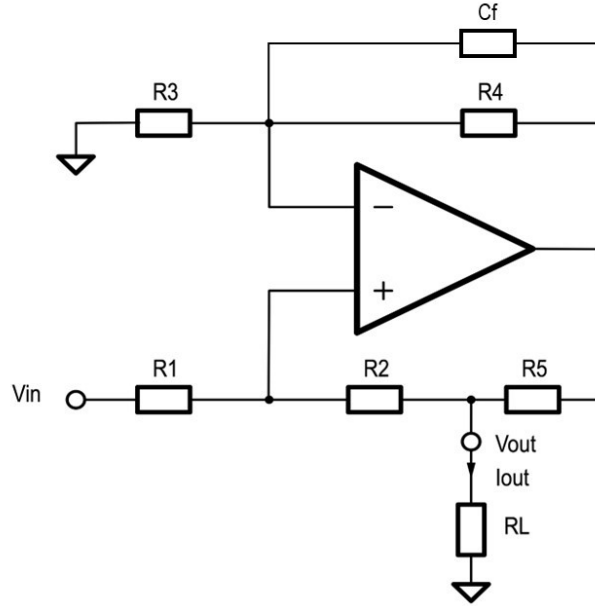


**Figure 4.3:** Configuration of the developed Improved Howland Current Pump which includes the feedback capacitor.

Resistor	Value
$R_1$	56 k $\Omega$
$R_2$	100 k $\Omega$
$R_3$	56 k $\Omega$
$R_4$	100 k $\Omega$ + 22 k $\Omega$ (Series)
$R_5$	22 k $\Omega$
$C_f$	10 pF

**Table 4.1:** Table of resistor and capacitor values of the circuit in Figure 4.3.

stay within the output swing limits of the chosen amplifiers, taking into account the load value within the range estimated from the impedance measurements previously discussed.

### Power supply

To ensure optimal performance of the chosen amplifiers, a dual supply of  $\pm 15$  V was provided for the LT1498 amplifier and  $\pm 18$  V for the OPA2892 using the Rigol DP832A DC Power Supply. Two 1  $\mu$ F capacitors were placed in parallel to each of

the two supply channels to enhance the quality and stability of the output voltage from the power source, reducing noise and improving overall system reliability.

### 4.3 Printed circuit board (PCB) design

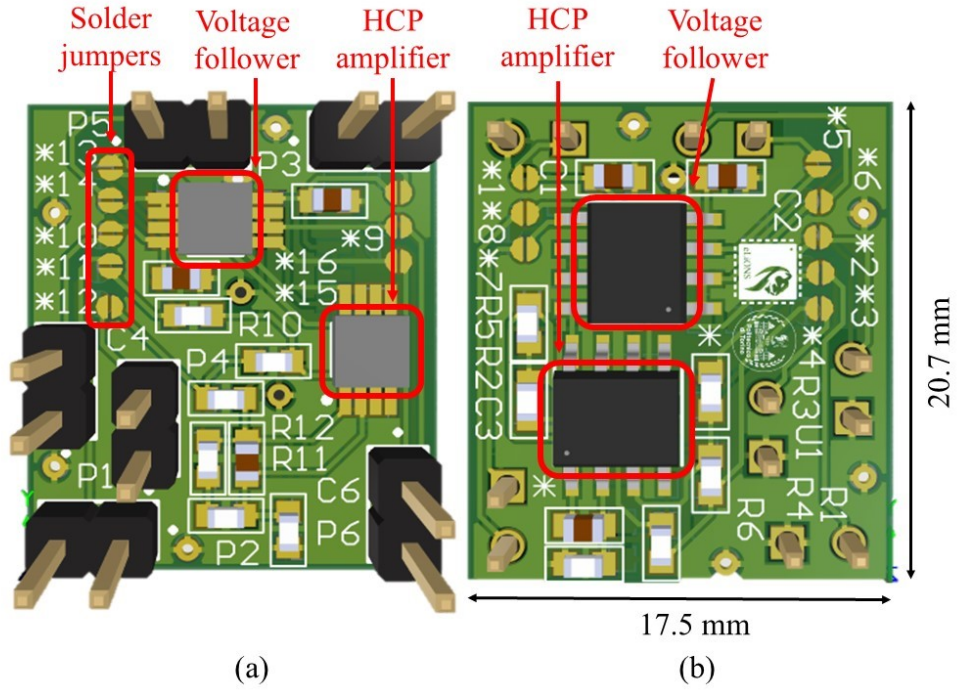


**Figure 4.4:** PCB layout showing an overview of (a) the top layer and (b) the bottom layer. The main components are highlighted in red.

To reduce the size of the system for wearable applications and minimize noise caused by wire connections, two identical Printed Circuit Boards (PCBs) were designed using Altium Designer®, as illustrated in Figure 4.4. The dual PCB configuration allows for the simultaneous acquisition of pulse wave signals from both the carotid and femoral arterial sites.

As previously mentioned, two operational amplifiers with high GBWP were identified as the optimal choice for the system. Two Howland Current Pump circuits were developed, each utilizing one of the selected amplifiers and identical resistance values. This design approach ensured that both circuits were thoroughly validated, allowing for the selection of the one with better performance for in vivo testing.

The first operational amplifier (OPA2892) was implemented on the top layer of

the PCB (Figure 4.4.b), while the second (LT1498) was placed on the bottom layer (Figure 4.4.a). For the voltage followers, an additional amplifier of the same model as the ones used in the Howland Current Pump was employed, as both amplifier packages include two independent amplifiers. The output of each voltage follower was connected to one of the two channels of the NiDAQ USB-6259 for differential signal acquisition.

Both circuits share the same pads for connection to the DC power supply, waveform generator and analog inputs of NiDAQ USB-6259, providing flexibility in operation. To facilitate the disconnection of one circuit from external devices, jumper soldering was incorporated on both the top and bottom layers. This design allows for easy switching between the two circuits, based on the specific testing needs.

The dimensions of the PCB are 20 mm x 20 mm, making the overall size of the hardware very compact. The PCB features 12 headers, enabling connections to external devices. These headers serve the following purposes:

- 3 headers provide power to the amplifiers ( $\pm V_s, GND$ ).
- 2 headers connect the inner electrodes to apply current to the tissues.
- 2 headers supply the input voltage signal to the Howland Current Pump ( $V_{in}, GND$ ).
- 2 headers connect the outer electrodes to the input of the voltage followers.
- The final 2 headers link the output of the voltage followers to the NiDAQ USB-6259 analog input channel for signal acquisition.

## 4.4 HCP validation test

Following the development of the two printed circuit boards, the Howland current pumps were submitted to a series of validation tests. The objective of these tests was to verify the independence of the output current from the load resistance, as well as to ensure that the amplitude corresponded to the theoretical value of 495  $\mu\text{A}$  when an input voltage signal of 5 V is applied.

The validation test was carried out by connecting resistors of known values as the load for the current generator and measuring the current flowing through the circuit with a multimeter placed in series with the load. The resistor values were chosen in the range 47  $\Omega$  to 6,800  $\Omega$  to ensure the inclusion of the tissue impedance value, while neglecting the capacitive component of the tissue impedance.

The results of the validation test are presented in the following section. As previously mentioned, to test each HCP contained in the PCB, it was necessary to solder the jumpers on the corresponding layer while removing the soldering on the opposite layer. This procedure was performed in order to disconnect one of the two HCPs from external devices.

#### 4.4.1 Results of HCP validation test

In the configuration previously stated ( $V_{in} = 5\text{ V}$ ,  $f = 50\text{ kHz}$ ), the measured values do not closely match the expected results. This can be observed in Figure 4.5, where the results of the validation test on the LT1498 are presented.

The current amplitude difference between the theoretical and measured values exceeds  $100\text{ }\mu\text{A}$  and does not appear to be independent of the load resistance. A slight decrease in amplitude is observed for resistances greater than  $2,700\text{ }\Omega$ , which is likely due to a combination of imperfect resistor matching caused by tolerance and the nonlinear behavior of the gain bandwidth product, both of which may degrade the output impedance of the Howland current pump.

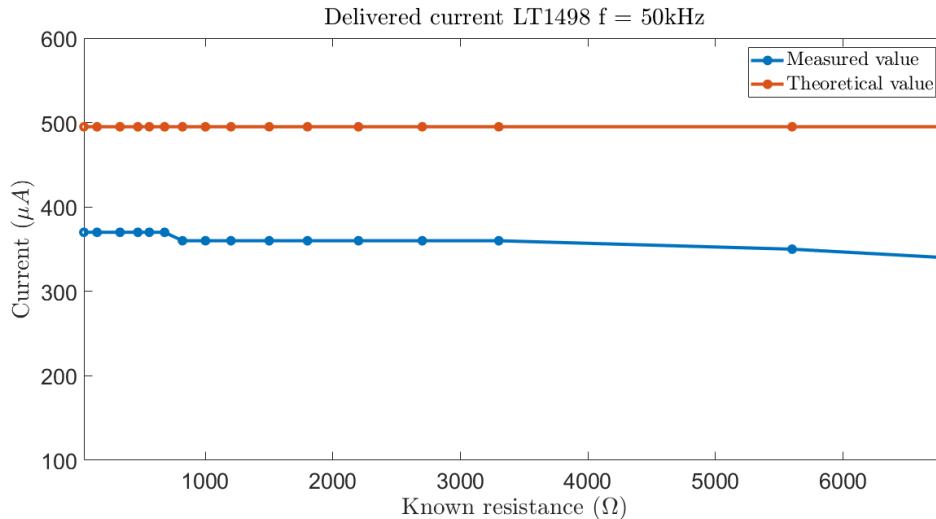


**Figure 4.5:** Theoretical vs. real behavior of the HCP using the LT1498, with an input voltage of  $5\text{ V}$  amplitude at a frequency of  $50\text{ kHz}$ .

It was therefore decided to test the HCP by applying a voltage signal at a lower frequency of  $20\text{ kHz}$ . Although the best resolution for detecting low impedance variations was found when the current signal was applied at  $50\text{ kHz}$ , [10], it is clear that a frequency of  $20\text{ kHz}$  is still sufficient to detect the pulse waveform, however, with a loss of resolution.

As shown in Figure 4.6 and Figure 4.7, there was an improvement in the Howland Current Pump performances for both the configuration (LT1498, OPA2892). The current is almost constant depending on the load resistance connected and the measured amplitude is closer to the theoretical value, the difference is about  $50\ \mu\text{A}$ .

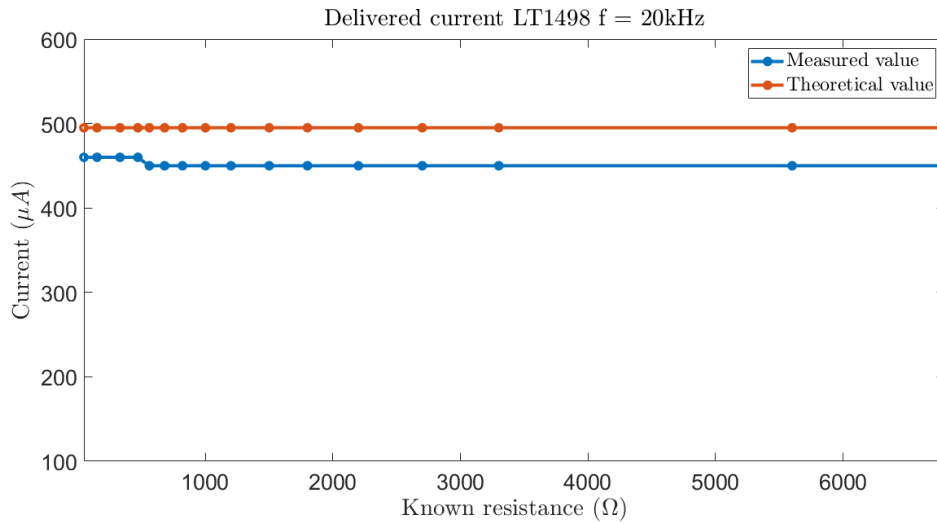


**Figure 4.6:** Theoretical vs. real behavior of the HCP using the LT1498, with an input voltage of 5 V amplitude at a frequency of 20 kHz.

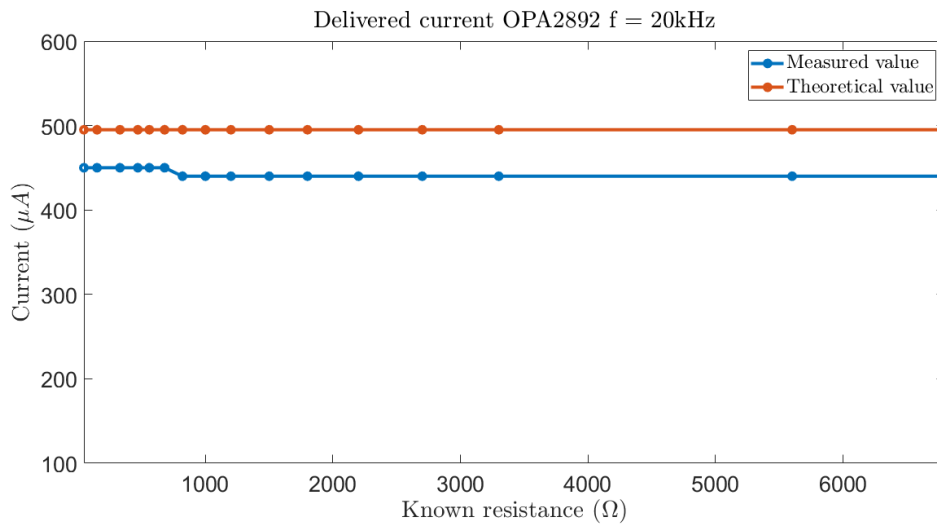


**Figure 4.7:** Theoretical vs. real behavior of the HCP using the OPA2892, with an input voltage of 5 V amplitude at a frequency of 20 kHz.

There was no evidence that the Howland Current Pump, when developed with

the OPA2892 amplifier (which has a GBWP of 2 GHz), outperforms the version using the LT1498 amplifier, which has a GBWP of 10 MHz. Moreover, during the validation test of the HCP featuring the OPA2892, overheating of the operational amplifiers was observed. This issue was likely caused by the fact that the amplifiers are designed for high-power applications, and although a thermal pad was included, the PCB's dimensions were insufficient to effectively dissipate the heat.

In view of the results that have been presented thus far, it has been determined that, in the event of equal performance, the system that features the LT1498 is more efficient than the alternative. Furthermore, the overheating issue that was identified in the validation test of OPA2892 poses a risk of accidental burns from skin contact, as the PCB will be placed as close as possible to the collection site.

## **4.5 Hardware assembly**

Subsequent to the verification of the stability and safety of the output current from the Howland Pump Current circuit using the LT1498 amplifier, the ECG cables for current injection and voltage acquisition were shortened with a view to reducing the distance between the PCB and the arterial site. These cables were then soldered directly to the corresponding headers on the PCB. Conversely, the cables supplying power and carrying the voltage input waveform were extended to position the external devices (acquisition board and power supply) on a stable plane, placed at a safe distance from the subject. In this case, the connections were not fixed by soldering.

# Chapter 5

## System implementation

In order to enhance the efficiency and reduce the time cost of electrode placement, a Graphical User Interface (GUI) was developed to observe the impedance signal during the setup process. The GUI includes real-time processing, dynamically displaying impedance values to guide the user in adjusting electrode placement. All of these aspects are further discussed in the following sections.

### 5.1 Impedance processing

The Graphical User Interface was created using the MATLAB® App Designer environment. Its main purpose is to display real-time signals, offering immediate feedback on sensor placement accuracy and the quality of the acquired pulse waves.

Since signals from two arterial sites can be collected simultaneously, the interface features two dedicated graphs. Each signal can be inverted using the *Invert* switch to display the familiar pattern, with a rapid rise during systole and a decrease during diastole. In reality, the physiological change occurs in the opposite direction: during systole, the increased blood volume in the aorta leads to a decrease in impedance, while during diastole, the reduced blood volume causes impedance to increase. This inversion feature makes the system more reliable. If the user reverses the order of the sensing electrodes, the signal polarity can be fixed directly through the GUI, without needing to physically reverse the electrodes.

The system allows users to acquire signals from either one or two channels for PWV computation. When using two channels, the NiDAQ USB-6259's two differential analog inputs are employed. The default sampling frequency is 100 kHz, but can be increased to 500 kHz when both channels are active.

The Graphical User Interface (GUI) also provides control over the Howland

Current Pump's input voltage waveform, with default settings of 20 kHz for frequency ( $f$ ) and 5 V for amplitude ( $V_{in}$ ). This setup is recommended because the hardware performs more stably at 20 kHz. Amplitudes exceeding 5 V may saturate the amplifier output due to the load impedance's uncertain characteristics.

Before to start the signal recording, the acquisition board must be configured by clicking the *CONNECT* button. At this point the *START* button is enabled and the system is ready to begin the acquisition.

During signal collection, users can mark specific time points as "events" using the *Trigger* switch. These events can be used for synchronization with other devices or for later analysis.

Finally, the GUI features a data-saving toolbox for storing unfiltered PW signals, along with options to configure sampling and output parameters, as well as manage recorded events for subsequent analysis.

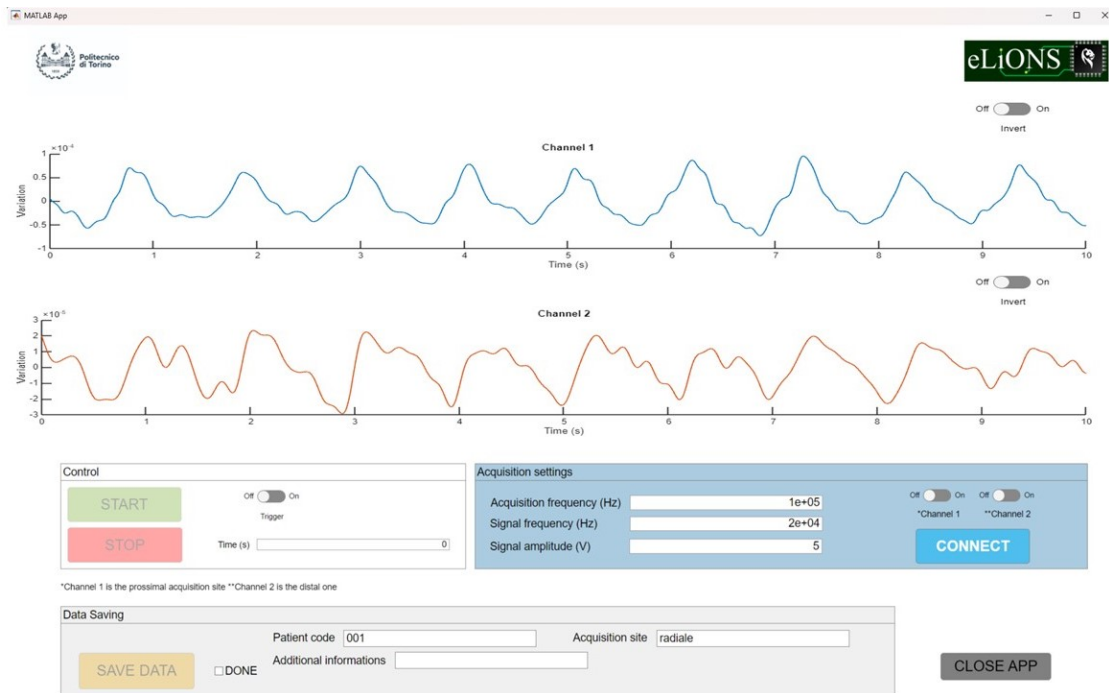


**Figure 5.1:** Main window of the implemented GUI, displaying the saving toolbox, pulse wave graphs, and acquisition controls. The *Trigger* and *Invert* switches are highlighted in red.

The subsequent section details the real-time processing and graphical visualisation of the bioimpedance signal.

### 5.1.1 Real time signal processing

As discussed in chapter 2, the pulsatile bioimpedance signal is embedded within the acquired voltage waveform; however, it must be extracted through demodulation.

In order to visualize the resulting signal in real-time, processing is performed on a buffer of the raw acquired waveform with a duration of 200 ms, as demonstrated in Figure 5.2. The current buffer is concatenated with the previous one, and the Fast Fourier Transform (FFT) is applied to 20 overlapping windows, each with a duration of 100 ms and an overlap of 10 ms. The peak spectrum corresponding to the frequency of the carrier signal (injected current) is extracted from the FFT of each window. This process enables the reconstruction of the modulating impedance signal, sampled at 100 Hz, while maintaining continuity between buffers and avoiding the loss of information.

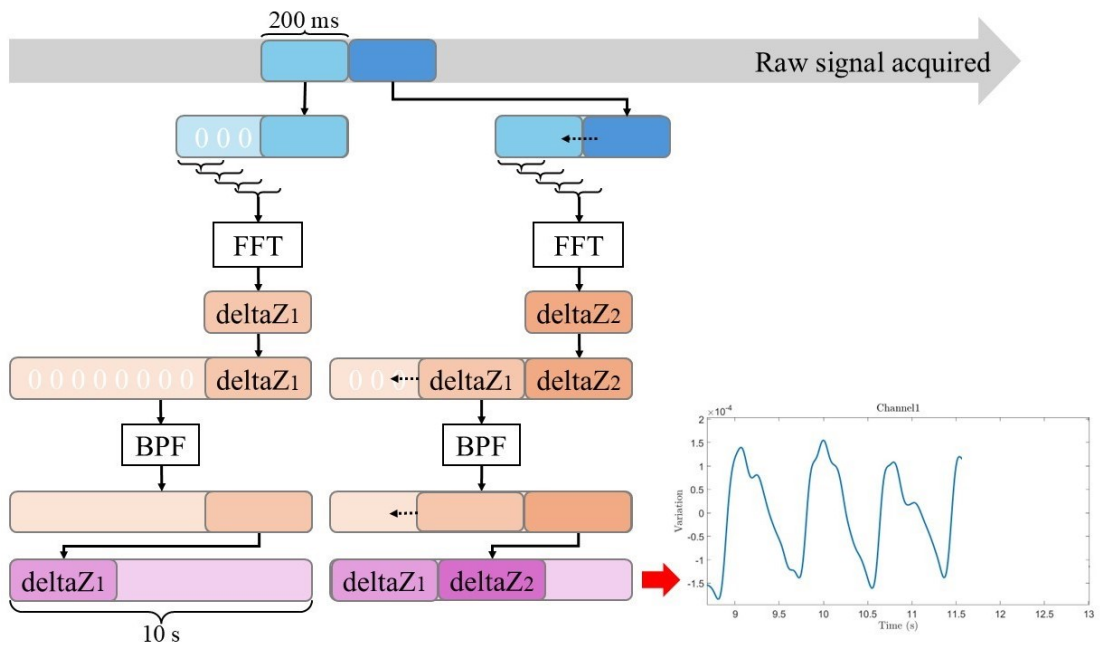


**Figure 5.2:** The image illustrates how the GUI reads the incoming data buffer, processes it in real-time, and displays the impedance variation signal.

After demodulation, the signal is cleaned up by removing unwanted high-frequency noise, the breathing pattern, and the constant baseline, all of which don't provide any useful information. Subsequently, the impedance variation signal is placed at the end of a vector with a length of 10 s. This vector is then filtered using a 4<sup>th</sup> order Butterworth band-pass filter with cutoff frequencies of 0.6 Hz and 15 Hz. To avoid the effects of filter transients due to the short buffer length, the

current buffer of the impedance signal is not filtered directly. Instead, the current buffer is shifted left by one block, and the filtered buffer is used to fill another vector, which is then plotted on the graph. The vector containing the data to plot is cleared every 10s. Each time the raw signal buffer is read and processed, the graph on the GUI is updated.

## Chapter 6

# In Vivo Experimental Validation

This section explains the aim of the in vivo experimental validation and the algorithms employed to analyze the processed data. It provides a clear overview of the data acquisition experimental protocol and concludes with the presentation of the results from the statistical analysis of the features extracted from the signals.

### 6.1 Preliminary Analysis

The in vivo test was conceived with the objective of evaluating pulse wave velocity through the simultaneous acquisition of pulse waves from the carotid and femoral arteries. The foot of each wave was identified, and the time delay between them was measured to compute the velocity, knowing the distance between the acquisition point. The primary objective of the study was to assess the reliability and accuracy of this method in relation to the standard electromechanical device.

Due to the difficulty in assessing the groin area crossed by the femoral artery, it was decided to proceed with testing only the feasibility of carotid pulse wave detection. Although the developed system allows for simultaneous acquisition, only one of the two PCBs was actually used.

To explore the correlation between the pulse wave signal obtained from the IPG-based device and the heart activity, the ECG signal of the subject was recorded simultaneously using *biosignalplex*.

## 6.2 Algorithms

The Intersecting Tangent Point and Pan-Tompkins algorithms were described in the following lines. Both the algorithms were implemented using MATLAB<sup>®</sup>.

### 6.2.1 Intersecting Tangent Point Algorithm

The Intersecting Tangent Point Algorithm is a computerized method to extrapolate the "foot" of the Pulse Wave signal. In literature studies, several points of the signal were investigated to compute the PWV, but the Intersect Tangent Point (ITP) results the most reliable and consistent among all the features that could be extracted in the arterial pulse (such as minimum, maximum, first derivate point, etc.) [46]. The ITP is defined as the projection on the signal of the point yielded by the intersection of a line tangent to the point of maximum first derivate of the pressure tracing and a horizontal line passing through the minimum before the start of the systolic peak. The algorithm includes the following step:

- First, the signal is filtered using a band-pass filter of 4<sup>th</sup> order with cut-off frequencies of 0.5 Hz and 10 Hz in order to remove the DC-offset, the high-frequency noise and the network interference from the signal.
- Then, a 4<sup>th</sup> order low pass filter at 2 Hz is applied in order to identify the numbers of blood pulses that occur in the signal under evaluation. The minimums of the filtered signal are considered the *events starters* and the number of samples in the mean cardiac period T is computed.

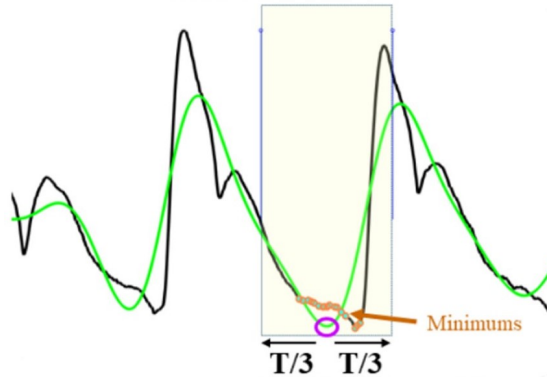


**Figure 6.1:** Minimums identification in the window  $\pm \frac{T}{3}$ , centered in the *event starter* [28].

- Signal windows of half length  $\frac{T}{3}$ , centered in each event starter, were considered. In this interval, all the minimums are identified and a threshold is defined

as 50% of the lowest minimum's y-coordinate among all the detected. The minimums that have a y-coordinate lower than the threshold value are saved in a *minimums buffer* (Figure 6.1).

- In order to compute the "foot" extraction, each blood pulse must be analyzed separately. A signal portion of T length is examined, starting from every *event starter*.
- The ITP extraction is carried out in the selected T-window. The first derivate of the signal is computed and its first maximum is identified. Since one point of minimum is needed, the closest to the maximum slope of the edge is taken. At this point, both the tangent passing through the maximum of the first derivate and the horizontal line through the minimum are traced. The "foot" of the pulse rising edge is the projection of the intersection between the two lines on the signal (Figure 6.2).

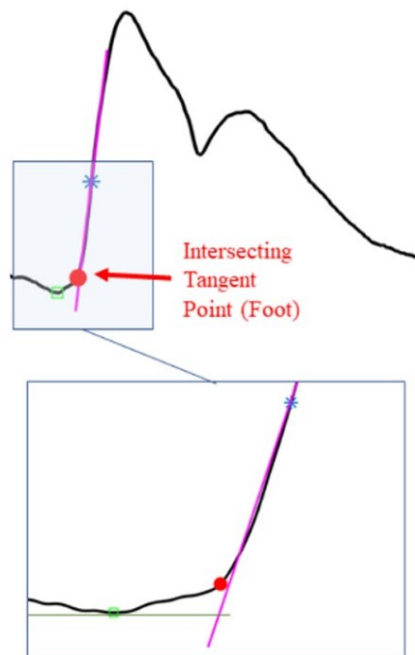


**Figure 6.2:** ITP definition as the projection on the signal of the intersection point between the tangent at the maximum of the first derivate and the horizontal line passing through the minimum [28].

## 6.2.2 Pan-Tompkins Algorithm

The Pan-Tompkins Algorithm is the most widely used for R peaks detection in ECG signals. It shows a high level of capability in handling of noisy ECG signals. The algorithm has two main stages: pre-processing and decision-making. In the pre-processing stage, the raw ECG signal is prepared for detection. This step involves removing noise, smoothing the signal, and enhancing the width and slope of the QRS complex. Then, the thresholds are used to only consider the signal peaks and eliminate the noise peaks in the decision stage [15]. The algorithm consists of the following steps:

- The average value of the raw ECG data is subtracted from the signal, which is then filtered. A low-pass filter and a notch filter are applied to eliminate high-frequency noise, such as interference from muscle activity and power line interference.
- The ECG signal was differentiated and normalized. In the derivative process, the low-frequency P- and T-waves are reduced to highlight the high-frequency signals found in the sharper slopes of the QRS complex.
- The signal was squared to ensure all components of the signal had positive values. This helped to further emphasize the higher amplitudes associated with the QRS complex. The squaring also helps to minimize the higher amplitudes from the T-waves, which could otherwise lead to false detections.
- The Moving Window Integration (MWI) is performed to acquire information from the waveform feature with the addition of the R- wave slope. A window with a width of 150 samples (150 ms) was used in this algorithm since the sample rate was 1,000 kHz.

The intermediate results of of Pan-Tompkins Algorithm pre-processing stage are shown in Figure 6.3.

Once the signal is pre-processed, the next step is the decision stage. This step is performed to decide whether or not the result of the MWI is a QRS complex by using an adaptive threshold. In the Figure 6.4 the results of QRS detection are shown.

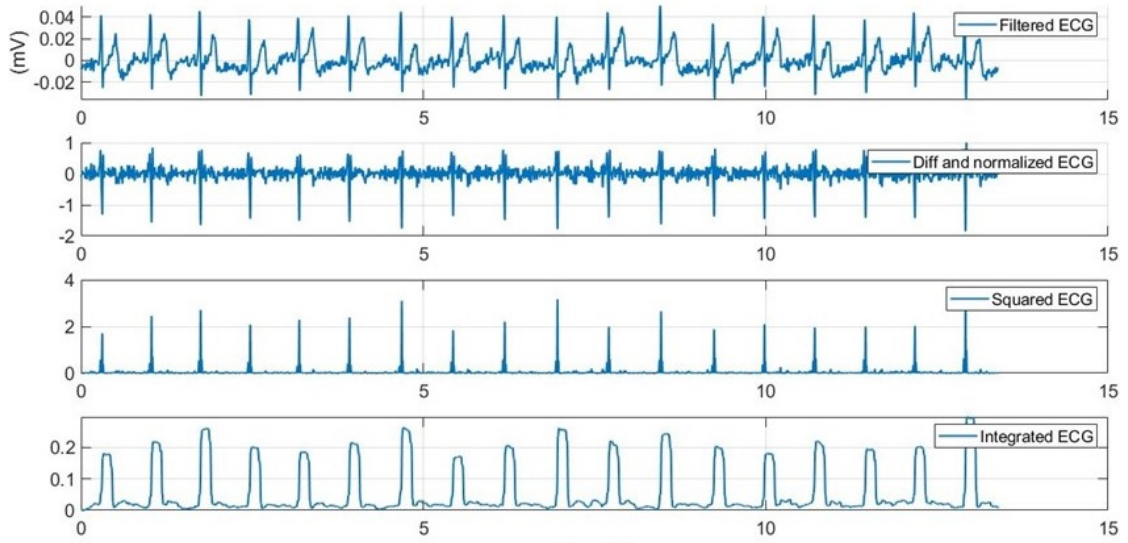


Figure 6.3: Intermediate results of Pan-Tompkins Algorithm pre-processing stage.

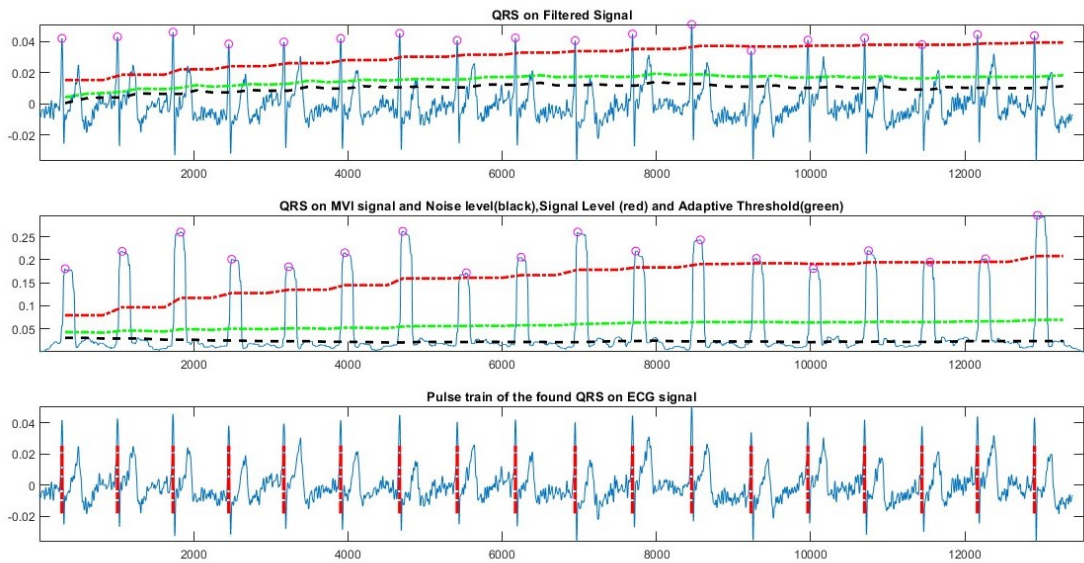
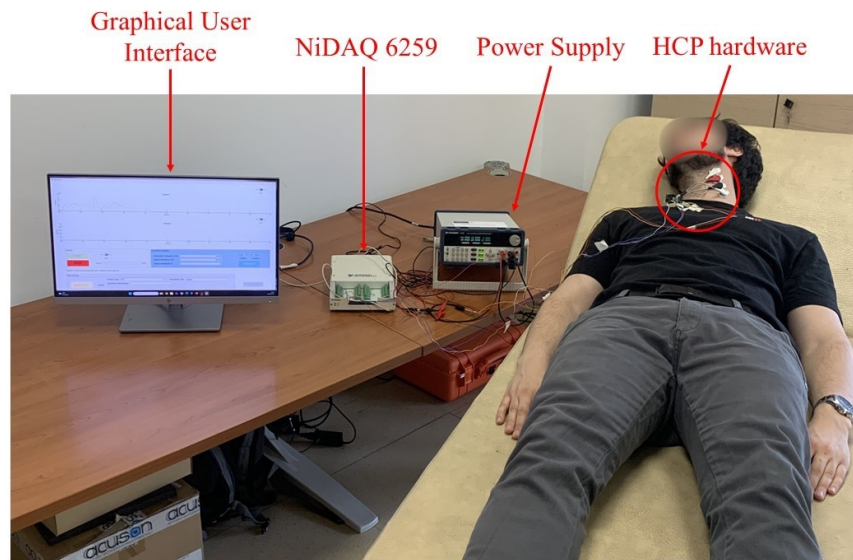


Figure 6.4: Final results of QRS detection using an adaptive threshold, green line in the graphs.

## 6.3 Experimental protocol

The in vivo test was conducted on four subjects to assess how the system's sensitivity in detecting the pulse varies depending on the subject. The subject is positioned supine during the acquisition (Figure 6.5).



**Figure 6.5:** In vivo test: recording setup. The main components of the setup are highlighted in red.

The excitation and sensing electrodes of the IPG-based device were placed parallel to the carotid axis, as illustrated in Figure 6.6. The optimal location was chosen by palpating the carotid artery with the fingertips. To minimize the detection of the respiratory component in the signal, due to the proximity of the carotid artery to the trachea, the sensor adhesive was resized. This adjustment reduced the interelectrode distance, which, in turn, made the current flux lines more superficial. A layer of adhesive thickness was maintained between the electrodes to prevent cross-talk between them.

The ECG acquisition was performed placing the three sensors as shown in the Figure 3.8. To accurately assess the correspondence between the two signals, synchronization is crucial. To achieve this, significant events from both recordings were identified and aligned across the two devices. For the IPG-based device, the *Trigger* switch in the GUI was used, while for the *biosignalplex*, a handheld switch was employed.

The NiDAQ USB-6259 was programmed to acquire signals from a single analog



**Figure 6.6:** IPG electrodes placement: the excitation electrodes are the outer coloured of white, while the sensing electrodes are the inner red and black.

input via the GUI, while the *biosignalplux* was configured for ECG registration by OpenSignals software.

By observing the IPG signal on the graphical user interface, the electrode placement was refined. Once a clear pulse wave signal was observed, an event was marked simultaneously on both devices. The recording was stopped after the final event was recorded.

The data and acquisition configuration were saved, with a specific code assigned to the subject.

## 6.4 Data processing

First, the ECG and IPG signals were synchronized based on the recorded time events.

The ECG data, originally given in ADC levels, needed to be converted to Volt. This conversion was done using the Equation 6.1 for the ECG signal provided in the datasheet [41].

$$ECG(V) = \frac{\left(\frac{ADC}{2^n} - \frac{1}{2}\right) \times VCC}{G_{ECG}} \quad (6.1)$$

where:

- $VCC = 3V$ , operating voltage;
- $n$  is the number of bits;
- $ADC$  is value sampled from the channel;
- $ECG(V)$  is the ECG value in Volt;
- $G_{ECG} = 1019$ , sensor gain.

After converting the ECG signal, it was filtered using a 4<sup>th</sup> order Butterworth band-pass filter with cutoff frequencies of 0.6 Hz and 100 Hz. Similarly, the unfiltered impedance signal was processed using a 4<sup>th</sup> order Butterworth band-pass filter with cutoff frequencies of 0.6 Hz and 10 Hz.

The R peaks in the ECG signal and the "foots" of the IPG waves (F) were identified, using the Pan-Tompkins algorithm and the Intersecting Tangent Point algorithm, respectively.

To demonstrate the correlation between the IPG and ECG signals it was decided to extract three significant parameters from the acquired signal (see Figure 6.7). For each subject were estimated:

- the delays between the "foots" of the IPG waves (F) and the R peaks of the ECG signal,
- the distances between the "foots" of the IPG waves (FF),
- the distances between the R peaks of the ECG signal (RR).

Subsequently, the differences between the RR and FF distances were calculated. The results of the validation test are presented below.

## 6.5 Results and statistical analysis

Two boxplots were produced for each subject to assess the results of the measurements described earlier.

Boxplots in Figure 6.8 collect the values of Pulse Arrival Time (PAT) for each subject, estimated using the "foot" of the pulse waves and R peaks of the ECG signal. The absolute value of the observations doesn't have clinical relevance because the two signals aren't perfectly synchronized due to the delay between the pressing of ECG bottom and the activation of *Trigger* switch on GUI. Despite this, the method

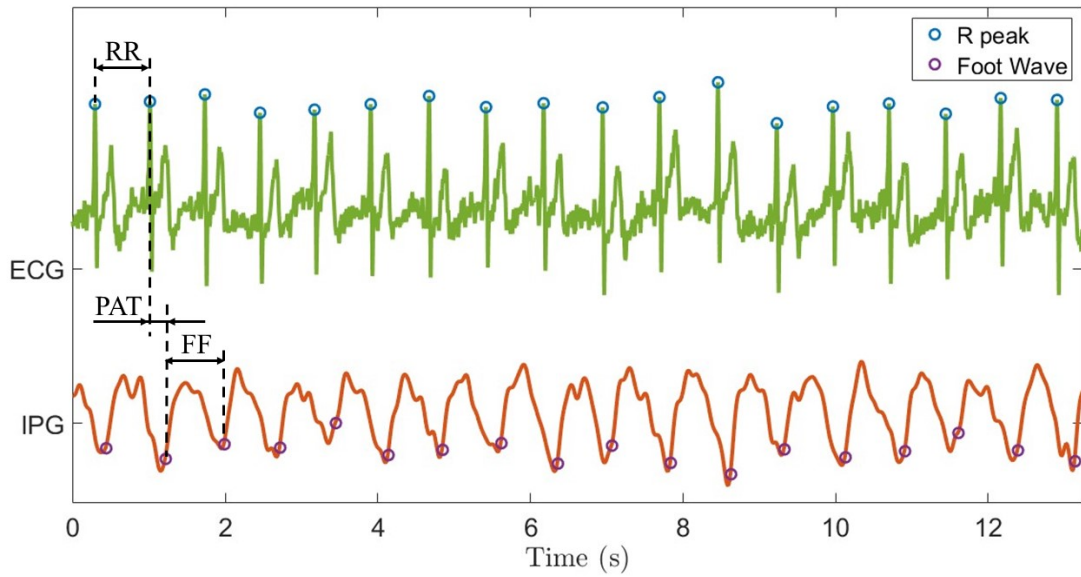


**Figure 6.7:** The recorded ECG and IPG signals are shown, along with the key parameters that were extracted.

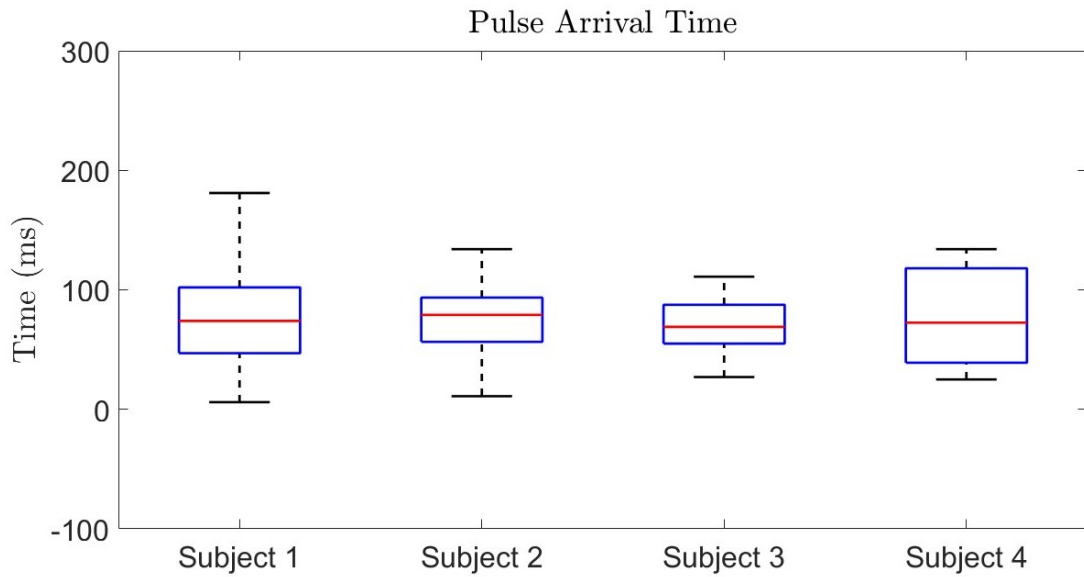


**Figure 6.8:** Boxplots of Pulse Arrival Time (PAT) measurements for each subject.

shows low variability: the interquartile range is at maximum lower than 100 ms. The highest precision results for the subject number 3, while increased variability

affects the distribution of the fourth subject's observations.

The second boxplot group in the Figure 6.9 shows the distributions of the differences between the RR and FF distances. The chart displays that these differences are almost zero for all subjects, meaning that the cardiac period can be evaluated equally well using either the IPG signal or the ECG signal.

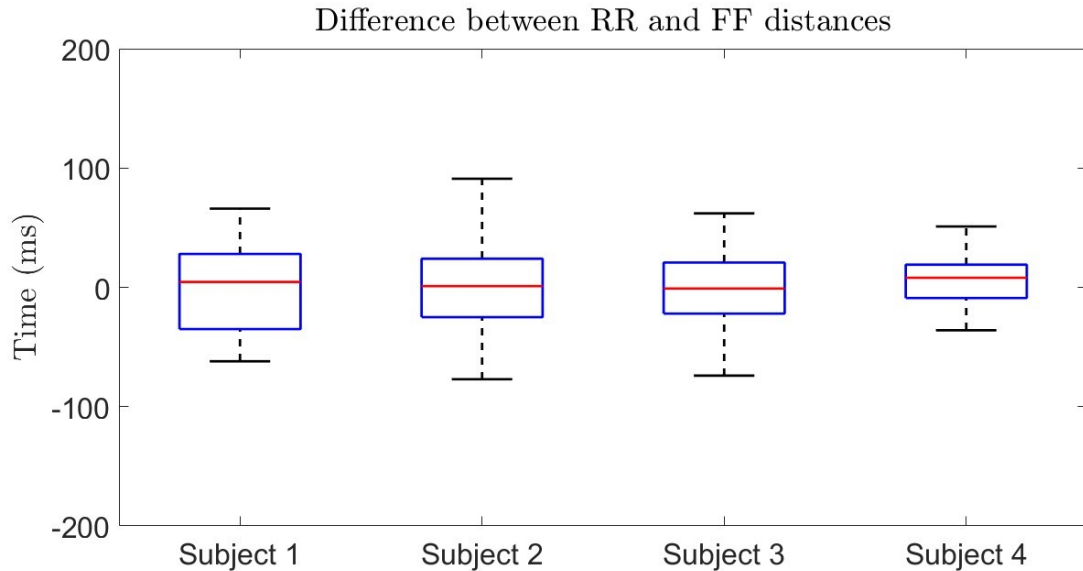


**Figure 6.9:** Boxplots RR-PP.

The outcomes of the statistical analysis, previously illustrated, prove the correlation between the bioimpedance wave and ECG signal. In the light of these findings, the impedance plethysmography technique appears a consistent and reliable method for pulse wave detection from the carotid artery.

# Chapter 7

## Conclusion

The main goal of the thesis project was to show that the Impedance Plethysmography (IPG) technique can be used for estimating Pulse Wave Velocity (PWV). This parameter is an index to evaluate the arterial stiffness that is a critical marker of cardiovascular health. Estimating the velocity at which the pulse wave travels through the arteries typically requires signals from two arterial sites, usually the carotid and femoral arteries. To address this, the developed system was designed for dual excitation, signal acquisition, and visualization. While the primary goal wasn't fully achieved due to challenges in assessing the femoral artery, the results are still promising. It was shown that the method implemented allows for pulse wave detection from the carotid artery. The statistical analysis also demonstrates that the recorded IPG signal is correlated with the ECG signal.

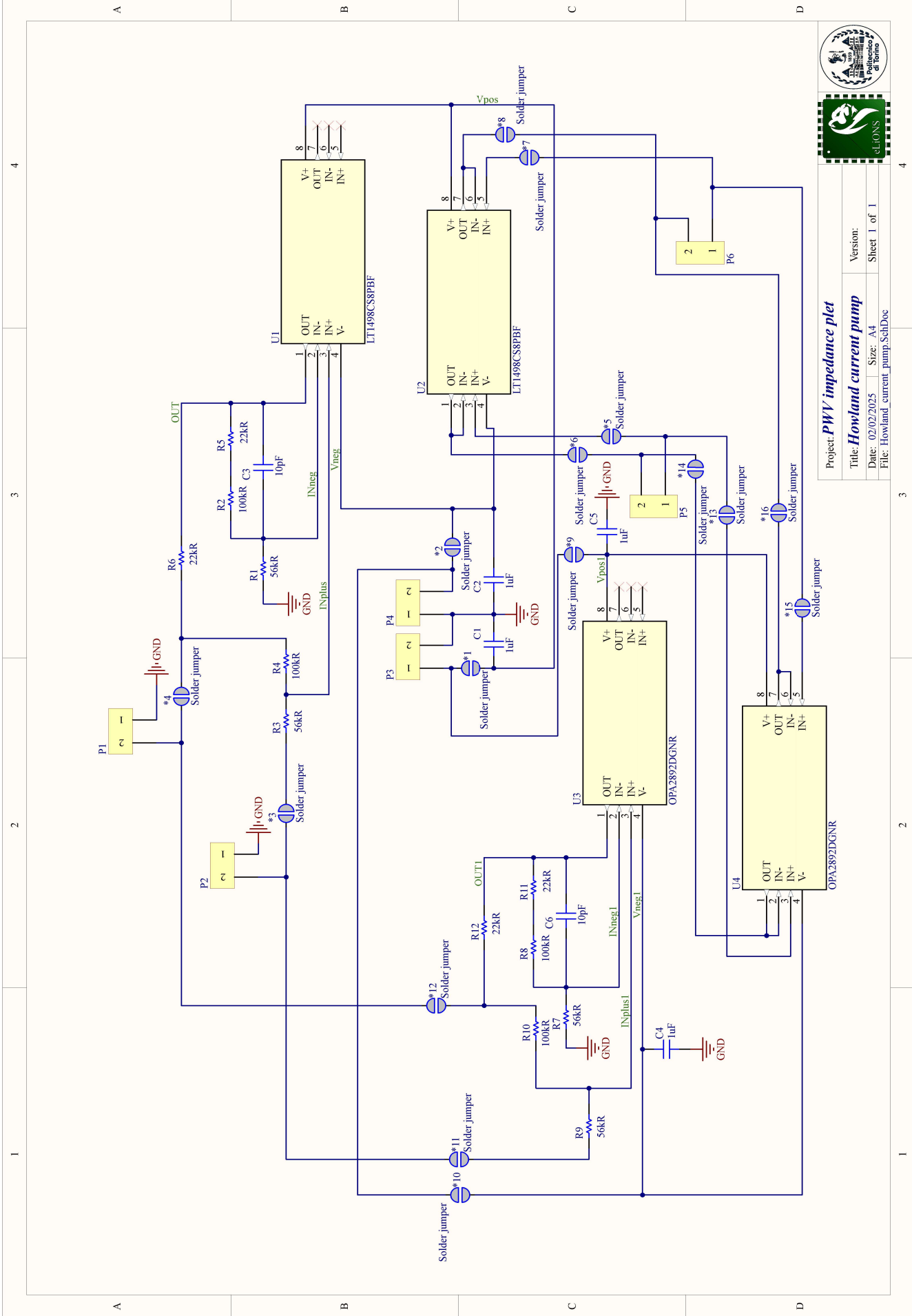
The creation of the Graphical User Interface (GUI), along with the real-time processing algorithm, improved the procedure for placing electrodes on the subject's skin. However, electrode placement is still an unresolved issue that needs to be addressed in future work. One potential solution could be to use a multi-electrode approach, which would allow for identifying the optimal configuration of excitation and acquisition electrodes from various options, without the need to physically move them.

Future improvements could include choosing a new amplifier for the Howland Current Pump to better stabilize the output current, which is currently influenced by the amplifier's CMRR, depending on the frequency of the input signal. In this way, the excitation signal frequency could be set to 50 kHz, which corresponds to the frequency where the greatest variation between diastolic and systolic pressure is detected.

In addition, future research could look into the possibility of using dry electrodes to create a wearable device.

# Appendix A

## Schematic



Project: **PWV impedance plet**  
 Title: **Howland current pump**  
 Date: 02/02/2025    Size: A4  
 File: Howland\_current\_pump.SchDoc

Version:	
Sheet 1 of 1	



# Bibliography

- [1] *Cardiovascular diseases (CVDs)*. URL: [https://www.who.int/news-room/fact-sheets/detail/cardiovascular-diseases-\(cvds\)](https://www.who.int/news-room/fact-sheets/detail/cardiovascular-diseases-(cvds)) (visited on 01/22/2025) (cit. on pp. 1, 23).
- [2] *Cardiac Disease - Creative Diagnostics*. URL: <https://www.creative-diagnostics.com/Cardiac-Disease.htm> (visited on 01/31/2025) (cit. on p. 1).
- [3] Gregory A. Roth et al. «Global Burden of Cardiovascular Diseases and Risk Factors, 1990–2019». In: *Journal of the American College of Cardiology* 76.25 (Dec. 22, 2020), pp. 2982–3021. ISSN: 0735-1097. DOI: 10.1016/j.jacc.2020.11.010. URL: <https://www.ncbi.nlm.nih.gov/pmc/articles/PMC7755038/> (visited on 01/23/2025) (cit. on pp. 2, 23).
- [4] Roma Pahwa and Ishwarlal Jialal. «Atherosclerosis». In: *StatPearls*. Treasure Island (FL): StatPearls Publishing, 2025. URL: <http://www.ncbi.nlm.nih.gov/books/NBK507799/> (visited on 01/23/2025) (cit. on pp. 2, 24).
- [5] Tânia Pereira, Carlos Correia, and João Cardoso. «Novel Methods for Pulse Wave Velocity Measurement». In: *Journal of Medical and Biological Engineering* 35.5 (2015), pp. 555–565. ISSN: 1609-0985. DOI: 10.1007/s40846-015-0086-8. URL: <https://www.ncbi.nlm.nih.gov/pmc/articles/PMC4609308/> (visited on 01/27/2025) (cit. on pp. 2, 29, 30, 34).
- [6] «(PDF) Intima media thickness, pulse wave velocity, and flow mediated dilation». In: *ResearchGate* (Oct. 22, 2024). DOI: 10.1186/1476-7120-12-34. URL: [https://www.researchgate.net/publication/264987129\\_Intima\\_media\\_thickness\\_pulse\\_wave\\_velocity\\_and\\_flow\\_mediated\\_dilation](https://www.researchgate.net/publication/264987129_Intima_media_thickness_pulse_wave_velocity_and_flow_mediated_dilation) (visited on 01/31/2025) (cit. on p. 3).
- [7] Helmut Hutten. «Impedance Plethysmography». In: *Encyclopedia of Medical Devices and Instrumentation*. John Wiley & Sons, Ltd, 2006. ISBN: 978-0-471-73287-7. DOI: 10.1002/0471732877.emd144. URL: <https://onlinelibrary.wiley.com/doi/abs/10.1002/0471732877.emd144> (visited on 01/29/2025) (cit. on pp. 2, 34).

- [8] Toan Huu Huynh, Roozbeh Jafari, and Wan-Young Chung. «Noninvasive Cuffless Blood Pressure Estimation Using Pulse Transit Time and Impedance Plethysmography». In: *IEEE transactions on bio-medical engineering* 66.4 (Apr. 2019), pp. 967–976. ISSN: 1558-2531. DOI: 10.1109/TBME.2018.2865751 (cit. on pp. 3, 37, 38, 41).
- [9] A. I. P. Wiegerinck, A. Thomsen, J. Hisdal, H. Kalvøy, and C. Tronstad. «Electrical Impedance Plethysmography Versus Tonometry To Measure the Pulse Wave Velocity in Peripheral Arteries in Young Healthy Volunteers: a Pilot Study». In: *Journal of Electrical Bioimpedance* 12.1 (Jan. 2021), pp. 169–177. ISSN: 1891-5469. DOI: 10.2478/joeb-2021-0020 (cit. on pp. 3, 37).
- [10] Ting-Wei Wang, Wen-Xiang Chen, Hsiao-Wei Chu, and Shien-Fong Lin. «Single-Channel Bioimpedance Measurement for Wearable Continuous Blood Pressure Monitoring». In: *IEEE Transactions on Instrumentation and Measurement* 70 (2021). Conference Name: IEEE Transactions on Instrumentation and Measurement, pp. 1–9. ISSN: 1557-9662. DOI: 10.1109/TIM.2020.3035578. URL: <https://ieeexplore.ieee.org/document/9247300> (visited on 01/31/2025) (cit. on pp. 3, 37, 38, 54).
- [11] Cindy L. Stanfield. *Principles of human physiology*. 5th ed. Boston: Pearson Education, 2013. 782 pp. ISBN: 978-0-321-81934-5 978-0-321-88461-9 (cit. on pp. 5–11, 15–20).
- [12] J. Gordon Betts et al. *20.1 Structure and Function of Blood Vessels - Anatomy and Physiology 2e | OpenStax*. Book Title: Anatomy and Physiology 2e Publisher: OpenStax. Apr. 20, 2022. URL: <https://openstax.org/books/anatomy-and-physiology-2e/pages/20-1-structure-and-function-of-blood-vessels> (visited on 02/01/2025) (cit. on pp. 6, 7).
- [13] *The ECG leads: Electrodes, limb leads, chest (precordial) leads and the 12-Lead ECG*. The Cardiovascular. URL: <https://ecgwaves.com/topic/ekg-ecg-leads-electrodes-systems-limb-chest-precordial/> (visited on 03/07/2025) (cit. on pp. 12, 13).
- [14] Satria Mandala, Tham Cai Di, Mohd Shahrizal Sunar, and Adiwijaya. «ECG-based prediction algorithm for imminent malignant ventricular arrhythmias using decision tree». In: *PLOS ONE* 15.5 (May 14, 2020). Publisher: Public Library of Science, e0231635. ISSN: 1932-6203. DOI: 10.1371/journal.pone.0231635. URL: <https://journals.plos.org/plosone/article?id=10.1371/journal.pone.0231635> (visited on 03/07/2025) (cit. on p. 13).
- [15] Author. *Abnormal Hemoglobins*. Ask Hematologist | Understand Hematology. Nov. 27, 2019. URL: <https://askhematologist.com/abnormal-hemoglobins/> (visited on 02/28/2025) (cit. on pp. 21, 64).

- [16] *Mechanisms of Plaque Formation and Rupture*. DOI: 10.1161/CIRCRESAHA.114.302721. URL: <https://www.ahajournals.org/doi/epub/10.1161/CIRCRESAHA.114.302721> (visited on 01/24/2025) (cit. on p. 25).
- [17] Julio A. Chirinos, Patrick Segers, Timothy Hughes, and Raymond Townsend. «Large-Artery Stiffness in Health and Disease: JACC State-of-the-Art Review». In: *Journal of the American College of Cardiology* 74.9 (Sept. 3, 2019), pp. 1237–1263. ISSN: 1558-3597. DOI: 10.1016/j.jacc.2019.07.012 (cit. on pp. 26, 27).
- [18] Niklas Pilz, Viktor Heinz, Timon Ax, Leon Fessler, Andreas Patzak, and Tomas Lucca Bothe. «Pulse Wave Velocity: Methodology, Clinical Applications, and Interplay with Heart Rate Variability». In: *Reviews in Cardiovascular Medicine* 25.7 (July 17, 2024), p. 266. ISSN: 1530-6550. DOI: 10.31083/j.rcm2507266. URL: <https://www.ncbi.nlm.nih.gov/pmc/articles/PMC11317333/> (visited on 01/27/2025) (cit. on p. 26).
- [19] Jordi Alastruey et al. «Arterial pulse wave modeling and analysis for vascular-age studies: a review from VascAgeNet». In: *American Journal of Physiology - Heart and Circulatory Physiology* 325.1 (July 1, 2023), H1–H29. ISSN: 0363-6135. DOI: 10.1152/ajpheart.00705.2022. URL: <https://www.ncbi.nlm.nih.gov/pmc/articles/PMC7614613/> (visited on 01/26/2025) (cit. on p. 26).
- [20] Luca Mesin et al. «Estimation of Aortic Stiffness with Bramwell–Hill Equation: A Comparative Analysis with Carotid–Femoral Pulse Wave Velocity». In: *Bioengineering* 9.7 (July 2022). Number: 7 Publisher: Multidisciplinary Digital Publishing Institute, p. 265. ISSN: 2306-5354. DOI: 10.3390/bioengineering9070265. URL: <https://www.mdpi.com/2306-5354/9/7/265> (visited on 01/27/2025) (cit. on pp. 27, 29).
- [21] object Object. «Expert consensus document on the measurement of aortic stiffness in daily practice using carotid-femoral pulse wave velocity». In: (). URL: [https://core.ac.uk/reader/43314821?utm\\_source=linkout](https://core.ac.uk/reader/43314821?utm_source=linkout) (visited on 01/27/2025) (cit. on p. 28).
- [22] Andrew L. Wentland, Thomas M. Grist, and Oliver Wieben. «Review of MRI-based measurements of pulse wave velocity: a biomarker of arterial stiffness». In: *Cardiovascular Diagnosis and Therapy* 4.2 (Apr. 2014), pp. 193–206. ISSN: 2223-3652. DOI: 10.3978/j.issn.2223-3652.2014.03.04 (cit. on p. 30).
- [23] Jordi Calabia, Pere Torguet, Maria Garcia, Isabel Garcia, Nadia Martin, Bernat Guasch, Diana Faur, and Martí Vallés. «Doppler ultrasound in the measurement of pulse wave velocity: agreement with the Complior method». In: *Cardiovascular Ultrasound* 9 (Apr. 15, 2011), p. 13. ISSN: 1476-7120. DOI: 10.1186/1476-7120-9-13 (cit. on p. 30).

- [24] *SphygmoCor Technology*. URL: <https://cardiex.com/sphygmocor-technology/> (visited on 01/28/2025) (cit. on p. 31).
- [25] *DiaTecne s.r.l./Products/PulsePen*. URL: <https://www.pulsepen.com/pulsepen.html> (visited on 01/28/2025) (cit. on p. 31).
- [26] *Complior / products*. URL: <http://www.complior.com/products,%20http://www.complior.com/products> (visited on 01/28/2025) (cit. on p. 32).
- [27] *Aortic Pulse Wave Velocity*. Arteriograph Company. URL: <https://tensiomed.com/measured-parameters/aortic-pulse-wave-velocity-pwvao/> (visited on 01/28/2025) (cit. on p. 33).
- [28] Irene Buraioli, Davide Lena, Alessandro Sanginario, Dario Leone, Giulia Mingrone, Alberto Milan, and Danilo Demarchi. «A New Noninvasive System for Clinical Pulse Wave Velocity Assessment: The Athos Device». In: *IEEE Transactions on Biomedical Circuits and Systems* 15.1 (Feb. 2021). Conference Name: IEEE Transactions on Biomedical Circuits and Systems, pp. 133–142. ISSN: 1940-9990. DOI: 10.1109/TBCAS.2021.3058010. URL: <https://ieeexplore.ieee.org/document/9351690> (visited on 01/22/2025) (cit. on pp. 32, 62, 63).
- [29] A. Valerio, I. Buraioli, A. Sanginario, D. Leone, G. Mingrone, A. Milan, and D. Demarchi. «Live Demonstration: Wireless Device for Clinical Pulse Wave Velocity Evaluations». In: *2022 IEEE Biomedical Circuits and Systems Conference (BioCAS)*. 2022 IEEE Biomedical Circuits and Systems Conference (BioCAS). ISSN: 2163-4025. Oct. 2022, pp. 247–247. DOI: 10.1109/BioCAS4905.2022.9948659. URL: <https://ieeexplore.ieee.org/abstract/document/9948659> (visited on 01/22/2025) (cit. on p. 33).
- [30] Shafa Aria et al. «Measuring Blood Pulse Wave Velocity with Bioimpedance in Different Age Groups». In: *Sensors* 19.4 (Jan. 2019). Number: 4 Publisher: Multidisciplinary Digital Publishing Institute, p. 850. ISSN: 1424-8220. DOI: 10.3390/s19040850. URL: <https://www.mdpi.com/1424-8220/19/4/850> (visited on 01/29/2025) (cit. on p. 34).
- [31] Tushar Kanti Bera. «Bioelectrical Impedance Methods for Noninvasive Health Monitoring: A Review». In: *Journal of Medical Engineering* 2014 (2014), p. 381251. ISSN: 2314-5137. DOI: 10.1155/2014/381251 (cit. on p. 35).
- [32] Amy Liao et al. «Impedance sensing device for monitoring ulcer healing in human patients». In: *Annual International Conference of the IEEE Engineering in Medicine and Biology Society. IEEE Engineering in Medicine and Biology Society. Annual International Conference 2015* (2015), pp. 5130–5133. ISSN: 2694-0604. DOI: 10.1109/EMBC.2015.7319546 (cit. on p. 35).

- [33] Frederick A. Anderson. «Impedance plethysmography in the diagnosis of arterial and venous disease». In: *Annals of Biomedical Engineering* 12.1 (Jan. 1, 1984), pp. 79–102. ISSN: 1573-9686. DOI: 10.1007/BF02410293. URL: <https://doi.org/10.1007/BF02410293> (visited on 01/30/2025) (cit. on p. 36).
- [34] N. De Pinho Ferreira, C. Gehin, and B. Massot. «A Review of Methods for Non-Invasive Heart Rate Measurement on Wrist». In: *IRBM* 42.1 (Feb. 1, 2021), pp. 4–18. ISSN: 1959-0318. DOI: 10.1016/j.irbm.2020.04.001. URL: <https://www.sciencedirect.com/science/article/pii/S1959031820300804> (visited on 01/30/2025) (cit. on p. 36).
- [35] Marc Hernández-Urrea, Ramon Casanella, Casimiro Javierre, and Oscar Casas. «An Easy-to-Use Hand-to-Hand Impedance-Based Sensor to Obtain Carotid Pulse Arrival Time». In: *IEEE Sensors Journal* 23.5 (Mar. 2023). Conference Name: IEEE Sensors Journal, pp. 5362–5369. ISSN: 1558-1748. DOI: 10.1109/JSEN.2022.3232985. URL: <https://ieeexplore.ieee.org/document/10007852> (visited on 02/05/2025) (cit. on pp. 38, 41).
- [36] Ignacio Vazquez Lam. «Analysis of Improved Howland Current Pump Configurations». In: (2020) (cit. on p. 41).
- [37] *NI 6259 Specifications - NI*. <https://www.ni.com>. URL: <https://www.ni.com/docs> (visited on 01/22/2025) (cit. on p. 44).
- [38] *Data Acquisition Toolbox*. URL: <https://it.mathworks.com/products/data-acquisition.html> (visited on 01/22/2025) (cit. on p. 44).
- [39] Keysight. *E4990A Impedance Analyzer, 20 Hz to 10/20/30/50/120 MHz*. Keysight. Section: Article Section. URL: <https://www.keysight.com/us/en/product/E4990A/impedance-analyzer-20-hz-10-20-30-50-120-mhz.html> (visited on 02/10/2025) (cit. on pp. 44, 45, 48).
- [40] *8-Channel biosignalsplux Kit*. PLUX Biosignals. URL: <https://www.pluxbiosignals.com/products/8-channel-biosignals-kit> (visited on 02/07/2025) (cit. on p. 45).
- [41] *Electrocardiography (ECG) Sensor*. PLUX Biosignals. URL: <https://www.pluxbiosignals.com/products/electrocardiography-ecg-sensor-1> (visited on 02/07/2025) (cit. on pp. 46, 67).
- [42] Keysight. *11059A Kelvin Probe Set*. Keysight. Section: Article Section. URL: <https://www.keysight.com/us/en/product/11059A/kelvin-probe-set.html> (visited on 02/10/2025) (cit. on p. 47).

- [43] Gautam Anand, Yang Yu, Andrew Lowe, and Anubha Kalra. «Bioimpedance analysis as a tool for hemodynamic monitoring: overview, methods and challenges». In: *Physiological Measurement* 42.3 (Apr. 6, 2021). ISSN: 1361-6579. DOI: 10.1088/1361-6579/abe80e (cit. on pp. 48, 49).
- [44] *LT1498 Datasheet and Product Info | Analog Devices*. URL: <https://www.analog.com/en/products/lt1498.html> (visited on 02/11/2025) (cit. on p. 50).
- [45] *OPA2892 | Buy TI Parts | TI.com*. URL: <https://www.ti.com/product/OPA2892/part-details/OPA2892DGNR> (visited on 02/11/2025) (cit. on p. 50).
- [46] Y. C. Chiu, P. W. Arand, S. G. Shroff, T. Feldman, and J. D. Carroll. «Determination of pulse wave velocities with computerized algorithms». In: *American Heart Journal* 121.5 (May 1991), pp. 1460–1470. ISSN: 0002-8703. DOI: 10.1016/0002-8703(91)90153-9 (cit. on p. 62).